Sci. Rep. Kanazawa Univ. **ARTICLES**
Vol. 68, pp. 25–82, 2025

Mutation-Induced Changes in Binding Affinity of Nsp3-SARS-Unique Domain (SUD): A Study on Indonesian SARS-CoV-2 Variants

Dedy RENDRAWAN*, Kazutomo KAWAGUCHI and Hidemi NAGAO*

Faculty of Mathematics and Physics, Computational of Science, Institute of Science and Engineering, Kanazawa University
Kanazawa, 920-1192, Japan

(Received January 3, 2025 and accepted in revised form February 13, 2025)

Abstract The SARS-Unique Domain of non-structural protein 3 (SUD-Nsp3) plays a crucial role in viral replication and immune evasion, making it a key target of antiviral therapies against SARS-CoV-2. However, the fast mutations in the Nsp3 protein, identified in 50% of cases, indicate a critical role in the virus's genetic evolution and potential impact on viral function [1]. This study explores predicted mutants of Indonesian SUD-Nsp3, including A76S-G77S-T266I, A76S, G77S-K175R, and D302G, by applying molecular dynamics simulations and binding free energy calculations to assess the impacts of ligand interaction, structural stability, and drug resistance. Mutant 1 (A76S-G77S-T266I) exhibits increased stability with GS-441524 and Remdesivir, indicating promising therapeutic efficacy. Furthermore, moderate stability with Remdesivir and Saquinavir is shown in mutant 3 (G77S-K175R); hence, it is a potential candidate for drug discovery. Mutant 4 (D302G) shows promising stability and efficacy with GS-441524 and Saquinavir; however, it raises the potential for drug resistance with Remdesivir. Mutant 2 (A76S) displays balanced binding stability and potential efficacy. Moreover, the structural analysis shows that mutants increased flexibility in the N and C domains, while the M domain remains structurally stable. Decomposition energy highlights critical residues that contributed to ligand binding, including PRO35, GLN102, and ARG237. This work optimizes therapeutic strategies against SARS-CoV-2 mutants toward improved drug efficacy and reduced resistance.

Keywords. Nsp3-SARS-Unique Domain (SUD); Mutations; Binding Free Energy; Molecular Dynamics; Drug Resistance; COVID-19.

1 Introduction

The COVID-19 pandemic has brought effective antiviral therapies, although the extensive research has still proven inadequate [2, 3]. Furthermore, the high mutation rate and genetic variance change

*Corresponding authors Email: Hidemi Nagao (nagao@wriron1.s.kanazawa-u.ac.jp); Dedy Rendrawan (dedyrendrawan@gmail.com, dedy@wriron1.s.kanazawa-u.ac.jp)

of SARS-CoV-2 pose a challenge to drug development that could enable the virus to enhance transmissibility, evade immunity, and develop resistance [4]. A previous genomic study in SARS-CoV-2 found various fundamental mutations. The mutations among them are nsp3 (50%), nsp4 (70.4%), nsp12 (99.3%), and spike (97.6%), with residue changes of P1228L, T4291, P323L, and D614G, respectively. Nonstructural protein 3 (Nsp3) is a fundamental multifunctional protein, especially in the SARS-Unique Domain (SUD). Its domain is critical for RNA translation, viral replication, and immune evasion [5, 6, 7, 8, 9, 10]. In this study, the SARS-CoV-2 virus with a high mutation rate could be emergent mutations that will continuously arise, particularly in fundamental proteins such as Nsp3-SUD. The emerging mutations might alter protein stability, interactions, and the efficacy of drugs. Co-variant and multiple sequence alignment (MSA) analyses effectively examine the evolutionary coupling of residues. They could also identify potential mutation hotspots within Nsp3-SUD, which might impact its structure and function in viral replication [11, 12]. Investigating a novel inhibitor development with various potential ligands, including GS-441524, Remdesivir, and Saquinavir, could give novel insights into understanding the stability of the structure of wild-type and mutant complexes [13, 14].

2 Materials and Methods

2.1 Dataset preparation and sequence retrieval

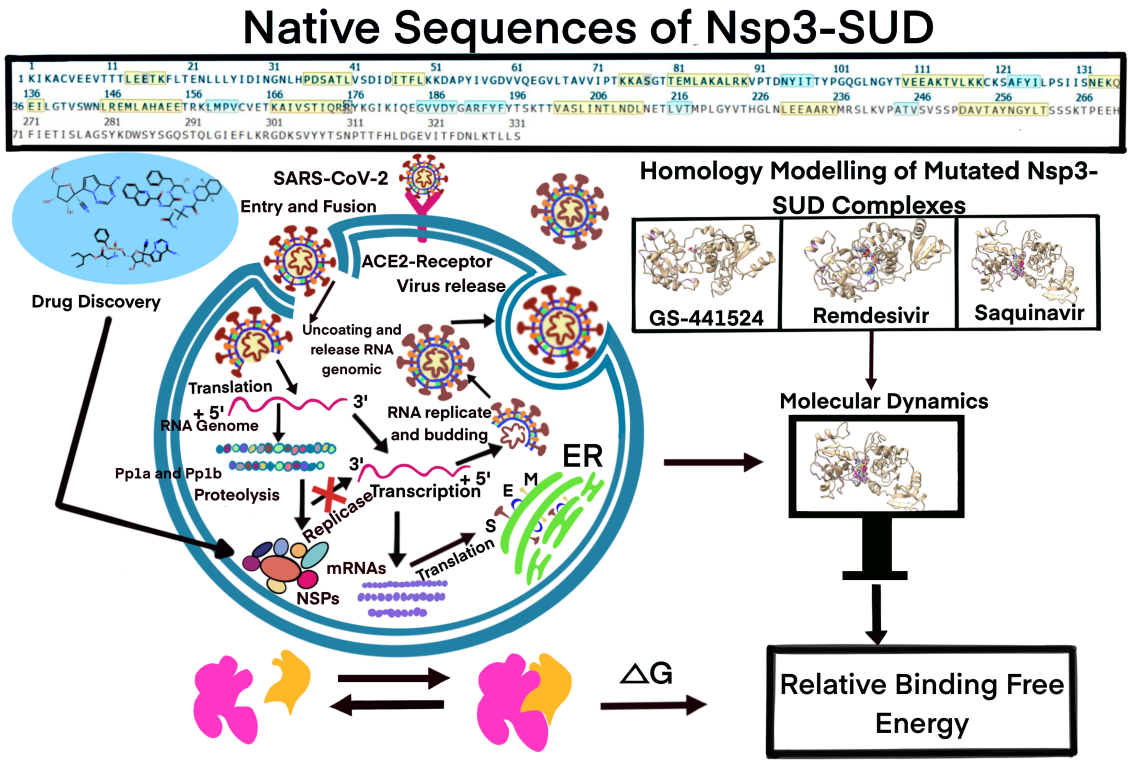

Figure 1: Material and Methods

Data used in this research methodology was obtained from the GISAID dataset considered Wuhan SARS-CoV-2 genome with accession no. NC-045512.2 as reference sequences (NCBI,

www.ncbi.nih.gov.) [15]. The full-length Indonesian SARS-CoV-2 genome sequences were downloaded in FASTA format from GISAID [16]. Unipro Ugene and the MAAFT G-INS-i algorithm have been optimized for similar sequences by reducing gaps and maintaining structural integrity. It was also used for multiple sequence alignment (MSA). The 90% mismatch threshold was set to identify the conserved region and give more priority to frequent residues changed within Nsp3-SUD [17, 18]. A wild-type three-dimensional Nsp3-SUD model was generated using I-Tasser and consisted of three domains (N, M, and C). Whereas Three-dimensional model constriction due to mutation of the Nsp3-SUD gene was done using FoldX5 software (www.foldxsuite.crg.eu), plugged into Yasara software (http//.www.yasara.org) [19]. Candidate drug potentials such as GS-441524, Remdesivir, and Saquinavir [13] would be assessed and applied to structural modeling and molecular dynamics (MD) simulations to study their impact on protein stability and interactions with drug efficacy.

2.2 Docking and Molecular Dynamics (MD) simulations

Docking and MD simulations were performed to evaluate protein-ligand interaction stability. Molecular docking was performed using AutoDock Vina integrated into the Chimera package, followed by ligand optimization and minimization [20]. The docking coordinates were X = 61.70, Y = 73.60, and Z = 65.50, with a box size of $12.70 \times 16.20 \times 21.00$, based on wild-type binding site predictions from I-Tasser Cofactor, H-Dock, and E-Dock [21]. Solution builder on CHARMM-GUI prepared complex proteins for molecular dynamic simulation through a CHARMM36 force field [22, 23]. The minimization and equilibration steps were performed for the complexes, followed by 100 nanoseconds (ns) production MD simulation at a temperature of 300 K and pressure of 1 atm using GROMACS 2022.2 Version [24]. C-Alpha of root mean square deviation (RMSD), root mean square fluctuation (RMSF), radius of gyration (Rg), solvent accessible surface area (SASA), and hydrogen bond (HB) are represented as graphs using MDAnalysis and fingerPrint Analysis plugins in the MDAnalysis Package [25, 26].

2.3 MMPBSA/MMGBSA binding-free energy calculations

Modern drug development focuses on advanced sampling methods and parameterized force fields in all-atom free energy simulations [27, 28]. Estimating thermodynamic or binding free energies is fundamental for improving innovation and efficacy in drug design and discovery [27, 29]. Calculations of the absolute binding free energy require enough computational resources, great consideration of restraining potentials, and valid intermediate states [30]. In the present study, binding free energy was estimated using the Molecular Mechanics/Poisson-Boltzmann Surface Area (MM/PBSA) and Molecular Mechanics/Generalized Born Surface Area (MM/GBSA) methods through 100 ns molecular dynamics simulations trajectories. The equations give the breakdown of the free energy of ligand-receptor binding into various energetic terms [31];

$$\Delta G_{\text{bind}} = \Delta G_{\text{complex}} - (\Delta G_{\text{receptor}} - \Delta G_{\text{ligand}}) \tag{2.1}$$

$$\Delta G_{\text{bind}} = \Delta E_{\text{MM}} + (\Delta G_{\text{sol}} - T\Delta S) \tag{2.2}$$

$$\Delta E_{\text{MM}} = \Delta E_{\text{bond}} + \Delta E_{\text{angle}} + \Delta E_{\text{dihedral}} + \Delta E_{\text{ele}} + \Delta E_{\text{vdW}} \tag{2.3}$$

$$\Delta G_{\text{sol}} = \Delta G_{\text{PB/GB}} + \Delta G_{\text{SA}} \tag{2.4}$$

$$\Delta G_{\text{bind}} = \gamma \cdot \text{SASA} + b \tag{2.5}$$

where in this calculation of binding free energy, $\Delta E_{MM}, \Delta G_{sol}$, and $-T\Delta S$ represent the energy contributions of the molecular mechanic's energy, the solvation free energy, and the entropy upon ligand binding, respectively (Eq. 2.2). The molecular mechanics energy ΔE_{MM} consists of five energetic terms, namely the bond (ΔE_{bond}), the angle (ΔE_{angle}), the dihedral ($\Delta E_{dihedral}$), the electrostatic (ΔE_{ele}), and the van der Waals (ΔE_{vdW}) energies (Eq. 2.3). In this study, we applied the single MD trajectory protocol for the end-point binding free energy calculation to ensure stable and reliable results. Under this approach, the bonded interactions, including ΔE_{bond}, ΔE_{angle}, and $\Delta E_{dihedral}$, effectively cancel out in the subsequent calculations. Consequently, it ΔE_{MM} is simplified as the sum of electrostatic ΔE_{ele} and van der Waals ΔE_{vdW} contributions. The solvation-free energy ΔG_{sol} consists of two components: the polar solvation energy ($\Delta G_{PB/GB}$) and the nonpolar solvation energy (ΔG_{SA}) (Eq.2.4). The polar contribution is computed using either the Poisson-Boltzmann (PB) or Generalized Born (GB) model, while the nonpolar component is estimated based on the solvent-accessible surface area (SASA) (Eq. 2.5) [32, 33, 34, 35].

3 Results and Discussion

3.1 Structural Comparison Analysis of Wild-Type and Mutant Nsp3-SUD Models

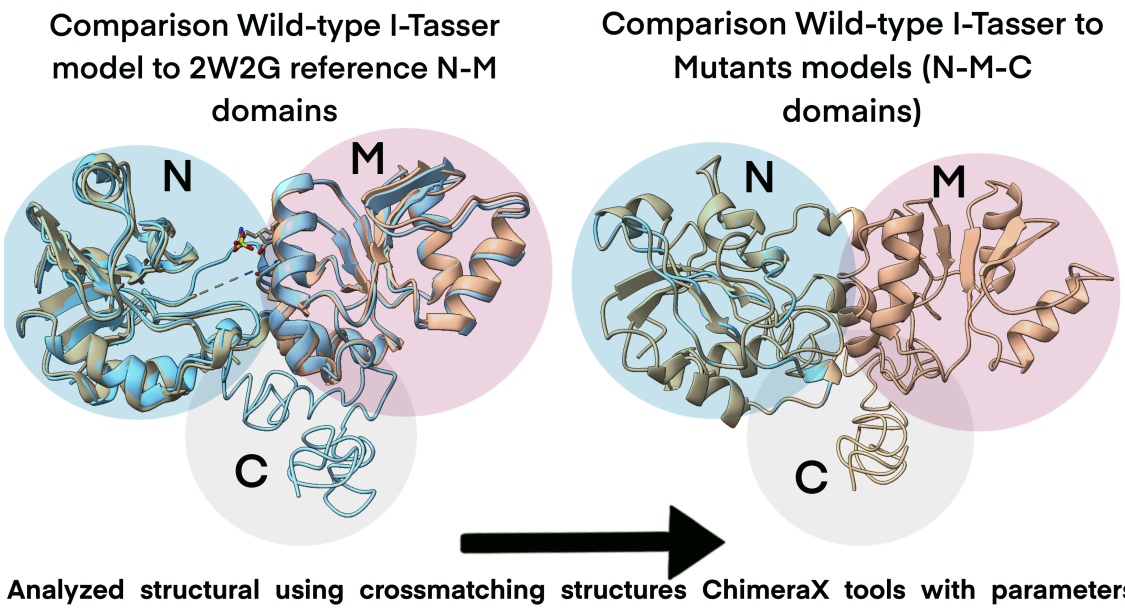

Analyzed structural using crossmatching structures ChimeraX tools with parameters chain pairing (bb), Alignment algorithm (Needleman-Wunsch), similarity matrix (BLOSUM-62), SS fraction (0.3); the matchmaker 2w2g to I-Tasser model chain A showed RMSD between 257 pruned atom pairs is 0.656 angstroms. Meanwhile, the second comparison between I-Tasser model to mutants models showed RMSD between 331 purned atom pairs is 0.000 angstroms. It's suggested similarity structures between reference to models both wild-type and mutants.

Figure 2: Structures Comparison between 2w2g.pdb chain A as reference N-M domains to wild-type I-Tasser model and mutants of Nsp3-SUD using matchmaker ChimeraX.

The effects of Indonesian mutations on the Nsp3-SUD were investigated using I-Tasser pre-

Table 1: Prediction of Indonesian mutations Nsp3-SARS-Unique Domain (Nsp3-SUD)

Wild-Type SUD-Nsp3	Changes of Residues
Mutation 1	A76S-G77S-T266I
Mutation 2	A76S
Mutation 3	G77S-K175R
Mutation 4	D302G

dicted models. Applying ChimeraX, the wild-type model was superimposed onto the experimental reference structure (2w2g.pdb, N-M domains; Figure 2) [36]. The comparison shows an RMSD of 0.656 (Å) over 257 pruned atom pairs, confirming a high degree of structural similarity to the template and suggesting significant similarities. The RMSD values remained close to 0.000 (Å) throughout all mutations, based on 331 pruned atom pairs. Sequence alignment analysis indicated high conservation, with mutant 3 (G77S-K175R) showing the highest similarity (1620.4) and mutant 4 (D302G) the lowest (1616.9). Mutants 1 (A76S-G77S-T266I) and 2 (A76S) showed an intermediate similarity of 1618.3 and 1617.6, respectively. These results indicated all the mutations in the Nsp3-SUD mostly show conserved structures. However, slight variations in sequence alignment scores could indicate localized structural or functional changes. Functional mutations in fundamental regions of proteins, such as ligand-binding sites, might potentially affect protein function and inhibit interaction with ligand compounds. Further studies will be needed to establish the biological implications of mutations for viral replication and the efficacy of drugs.

3.2 Mutations and structural shift Nsp3-SUD proteins

Nsp3 is the largest protein domain in the coronavirus genome, comprising 1922 amino acids. It is an essential protein in SAR-CoV-2 replication and transcription complexes [37]. This study considers the SARS-Unique Domain (SUD) Nsp3 mutants specific to Indonesian sequences (Table 1) using homology modeling (I-Tasser model) [21] concerning observing structural and functional implications. Indonesian Nsp3-SUD sequences and multiple sequence alignment (MSA) were aligned using the MAAFT algorithm integrated into the UniPro UGENE tool [17, 18]. The covariance method provides significant insight into residues' evolutionary coupling and functional importance. Four significant mutations, based on covariant relationship and potential to influence the structural stability or binding interactions [11, 12] are A76S-G77S-T266I, A76S, G77S-K175R, and D302G. The polarity mutation A76S provided an extra hydrogen bond effect to increase local stability. The mutation G77S-K175R enhanced electrostatic, hydrogen bond interaction, and ligand binding affinity. A76S-G77S-T266I is a combination substitution that indicates strong hydrophobic and hydrogen bond interactions, providing higher stability of binding affinity. The D302G mutation reduced regional polarity, potentially destabilizing electrostatic interactions.

3.3 Structural Stability and Ligand Dynamics of SARS-CoV-2 Nsp3 SUD Complexes

The 100 ns Molecular Dynamics (MD) simulations were performed to understand the stability and dynamics of the structure Nsp3-SUD binding to GS-441524, Remdesivir, and Saquinavir complexes. The effects of mutations were analyzed by RMSD, Rg, SASA, and hydrogen bonds, representing the wild-type and mutant proteins.

Mutant 1 (A76S-G77S-T266I) exhibited the most stable RMSD values of 5-7 (Å) across all domains and 3-5 (Å) in the N-M domain. Mutants 2 (A76S) and 4 (D302G) displayed moderate

stability. In contrast, the wild-type showed higher variability, with RMSD values from 6 to 10 (Å), while mutant 3 (G77S-K175R) was the least stable, exhibiting fluctuations as high as 8-10 (Å). The SASA values observed that the wild-type had higher solvent exposure at $\sim$ 195 nm^2. The most expanded structure could be observed for mutant 3, with the highest SASA of $\sim$200 nm^2. Rg values at $\sim$23.5 (Å) confirmed the compactness of the wild-type. The stability conformations are slightly expanded, as shown in mutants 1 and 2 Rg values of $\sim$24-25 Å. In contrast, mutant 3 was strongly destabilized, as indicated by the fluctuating Rg values between 26-28 (Å), suggesting a loss of compactness. Hydrogen bond analysis showed significant stability differences between the mutants. The wild-type, mutants 1 and 4, had maintained robust hydrogen bond interactions. It contributes to the overall stability of protein ligands, especially GS-441524 and Remdesivir complexes. Meanwhile, the reduction of hydrogen bonds might be related to various structural instabilities and loss of ligand-binding interaction, particularly shown in the mutant 3 Saquinavir complex.

Generally, mutants 1 and 4 are more stable with reduced solvent exposure and hence strong hydrogen bond interactions. Although mutant 3 leads to a loss of ligand binding stability, which indicates destabilization.

3.4 Binding Free Energy of Mutated Nsp3-SUD and WT

3.4.1 MM/PBSA and MM/GBSA Calculations

This study investigates the impact of binding ligand interaction in mutations of SARS-CoV-2 Nsp3-SUD proteins by applying MM/PBSA and MM/GBSA calculations. It is revealed by Table 2 and Figure 3 that the binding stability of GS-441524, Remdesivir, and Saquinavir complexes has been considerably altered due to the mutations.

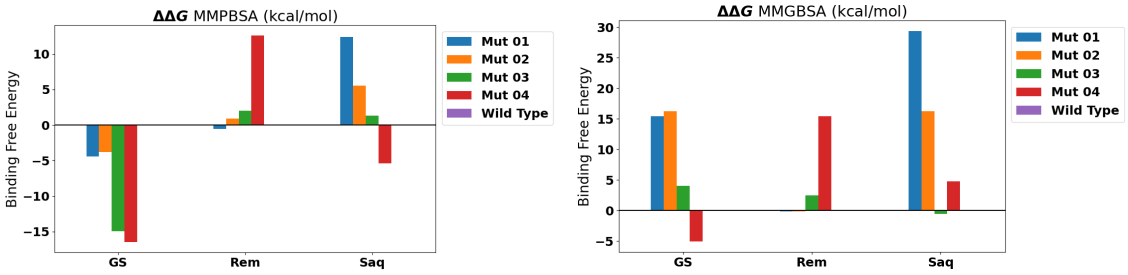

(a) MMPBSA Calculations. (b) MMGBSA Calculations.

Figure 3: Binding Free Energy Calculation Using (a) MMPBSA and (b) MMGBSA Methods.

The binding affinity analysis of GS-441524 indicated that mutants 1 and 2 exhibit significant instability, while mutant 3 demonstrates moderate stability, and mutant 4 presents the strongest stability. This trend is persistent with relative binding free energy calculations, confirming the mutation's stability differences. This study also indicated the risk resistance from low to high in mutants 4, 3, 2, and 1, respectively, with GS-441524 complexes. Remdesivir complexes demonstrated the lowest values of BFE in mutant 1, suggesting that low risk could be resistance. Furthermore, moderately favourable binding showed in mutants 2 and 3, which indicated resistance potential. Moreover, mutant 4 exhibits the weakest binding, which means significant instability and the highest resistance risk. Finally, Saquinavir contributed to the stabilization of Mutant 4, which formed the most stable complex, suggesting minimal resistance risk. Mutants 3 and 2 fol-

lowed with moderate affinity stability, also indicating a low risk of resistance. Mutant 1 showed highly destabilization binding interactions, suggesting a slight increase in the binding of mutant 3 with the ligand of saquinavir. On the other hand, mutant 4 also contributed to destabilization, potentially leading to higher resistance.

The analysis reveals that specific mutations influence ligand binding affinity. In GS-441524 complexes, all mutants enhanced relative binding energy, while in the Remdesivir complex, mutant 1 increased the binding stability. Similarly, in the Saquinavir complex, mutant 4 exhibits improved relative binding energy with minimal impact on other ligands, making it a promising candidate for GS-441524-based treatments. In contrast, mutants 2 to 4 in the Remdesivir complex and mutants 1 to 3 in the Saquinavir complex exhibited destabilizing relative binding, raising concerns about their therapeutic potentia These findings provide critical insights into drug discovery and the challenges posed by mutation-induced resistance.

Table 2: Binding free energy calculations (ΔG) (kcal/mol) for SARS-CoV-2 Unique Domain (SUD) complexes using MM/PBSA and MM/GBSA methods.

Complex	**MM/PBSA (kcal/mol)**	**MM/GBSA (kcal/mol)**
Wild-Type-GS SUD-Nsp3	-10.40	-29.53
Wild-Type-Rem SUD-Nsp3	-21.91	-23.70
Wild-Type-Saq SUD-Nsp3	-34.24	-48.52
Mutant-1-GS: A76S-G77S-T266I	-14.83	-14.13
Mutant-1-Rem: A76S-G77S-T266I	-22.45	-23.83
Mutant-1-Saq: A76S-G77S-T266I	-21.85	-19.17
Mutant-2-GS: A76S	-14.19	-13.31
Mutant-2-Rem: A76S	-20.99	-23.82
Mutant-2-Saq: A76S	-28.69	-32.29
Mutant-3-GS: G77S-K175R	-25.33	-25.47
Mutant-3-Rem: G77S-K175R	-19.92	-21.24
Mutant-3-Saq: G77S-K175R	-32.95	-49.12
Mutant-4-GS: D302G	-26.89	-34.63
Mutant-4-Rem: D302G	-9.33	-8.25
Mutant-4-Saq: D302G	-39.61	-43.72

3.4.2 Contribution Energy Decomposition Per-Residue in Mutants and WT Nsp3-SUD Protein bind to GS-441524 Nucleoside Core as Inhibitor

Energy decomposition analysis for the complexes of GS-441524 with wild-type and mutant Nsp3-SUD proteins revealed some key residues contributing to the stability of binding affinity, as indicated in Figure 4 and Supplementary Table 3. Interestingly, the residue PRO35 acts as a destabilizer in wild-type, although it is a major stabilizer in all mutants, especially in mutant 1 with the highest values. Conversely, ASP36 made minor contributions in the wild-type, mutants 1, and 3, likely due to local environmental changes that reduced ligand affinity. However, in mutant 3, ASP36 enhanced stabilization, suggesting a less disruptive effect on binding. The key residue GLN102 exhibited increased stabilization across all mutants. Additionally, mutants 1 and 3 demonstrated favorable structure integrity with strong electrostatic interactions. In contrast, residues ARG237 and SER238 showed decreased stability in all mutants, particularly mutants 2

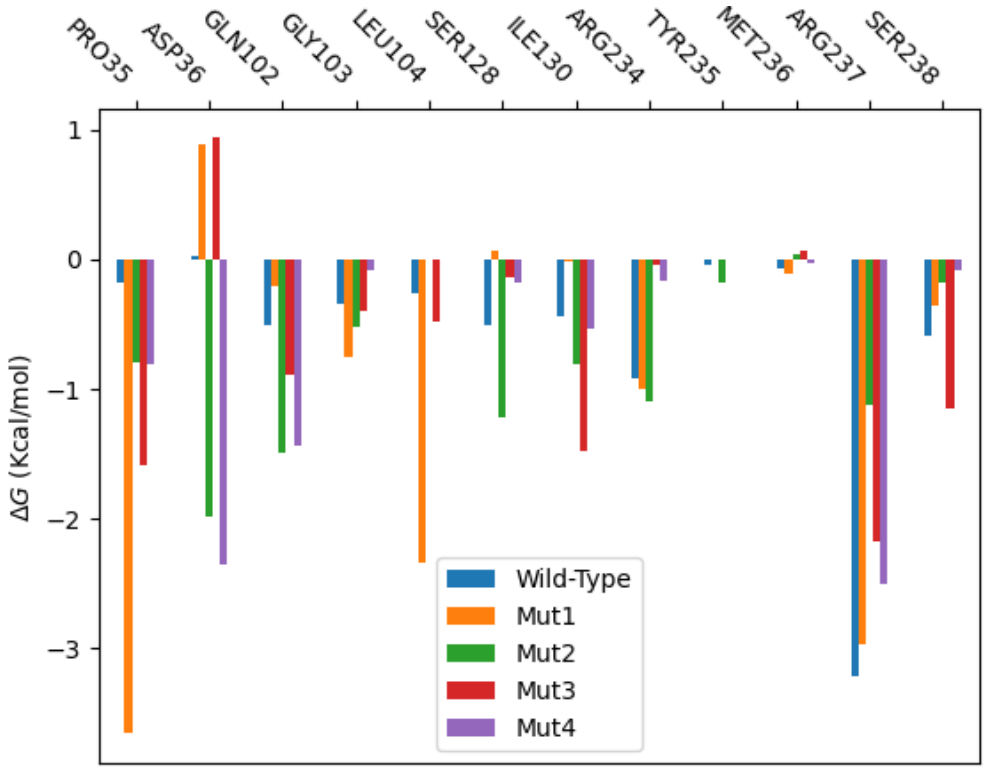

Figure 4: Energy Decomposition Per-Residues bound to GS-441524

and 3, indicating interference with fundamental binding interactions. Other key binding residues affected by various mutations include GLY103, LEU104, and TYR235. In general, PRO35 and GLN102 play a crucial role in stabilizing the binding affinity of GS-441524 mutant complexes.

3.4.3 Contribution Energy Decomposition Per-Residue in Mutants and WT Nsp3-SUD Protein bind to Remdesivir as Inhibitor

Wild-type and mutant Nsp3-SUD-bound Remdesivir protein complexes were analyzed using energy decomposition analysis (see Figure 5 and Supplementary Table 4). The residues contributing to binding stability provide key insights into the structural factors driving protein-ligand interactions. Among these residues, PRO35 was destabilized in wild-type complexes but emerged as the most stabilizing residue in mutant complexes, especially mutant 1, except mutant 4. Structural adjustment in the mutant complexes enhanced protein-ligand interaction, thereby maintaining stable binding site configurations. GLN102 residue consistently played a crucial role in stabilizing the protein-ligand mutant complexes, especially in mutants 1 and 3. This stabilization might result from hydrogen bonding or electrostatic interactions with Remdesivir, which strengthen binding stability and preserve the structural integrity of the binding pocket, which is critical for efficient ligand recognition and binding affinity. Conversely, residue ARG237 exhibited a reduced stabilizing effect in mutant 2, wild-type, and mutant 4, indicating an extended unfavorable binding energy contribution. Further conformational modifications of Remdesivir complexes might reduce binding stability. The residues such as LEU130 and SER238 in mutant 4 were shown to be destabilized due to conformational changes that interfere with the increased binding affinity. In

contrast, ARG234, TYR235, and especially LYS240 exhibit mixed effects. A few mutations are slightly stable, while other results show unstable contributions. That suggested a given mutation might have a dependent influence and consequently various effects on binding stability.

The analyses underline the fundamental key residue stabilizer protein-ligand complexes such as PRO35, GLN102, and ARG237. In contrast, residues ASP28 and LYS240 showed unstable effects, indicating their potential role in reducing binding stability.

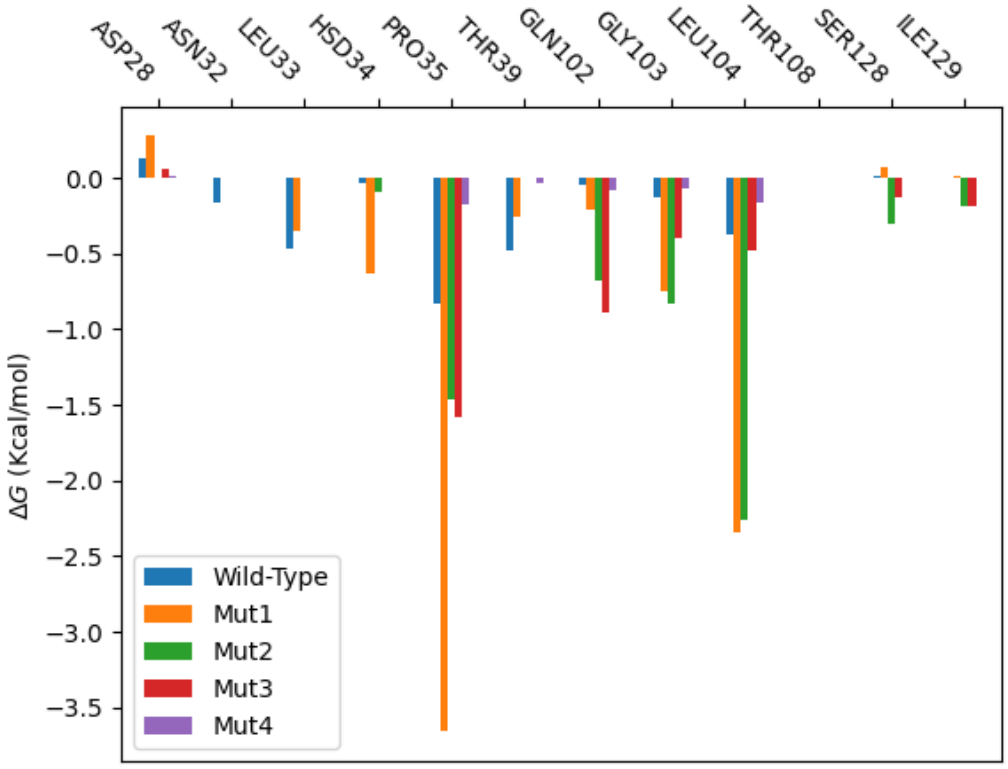

(a)

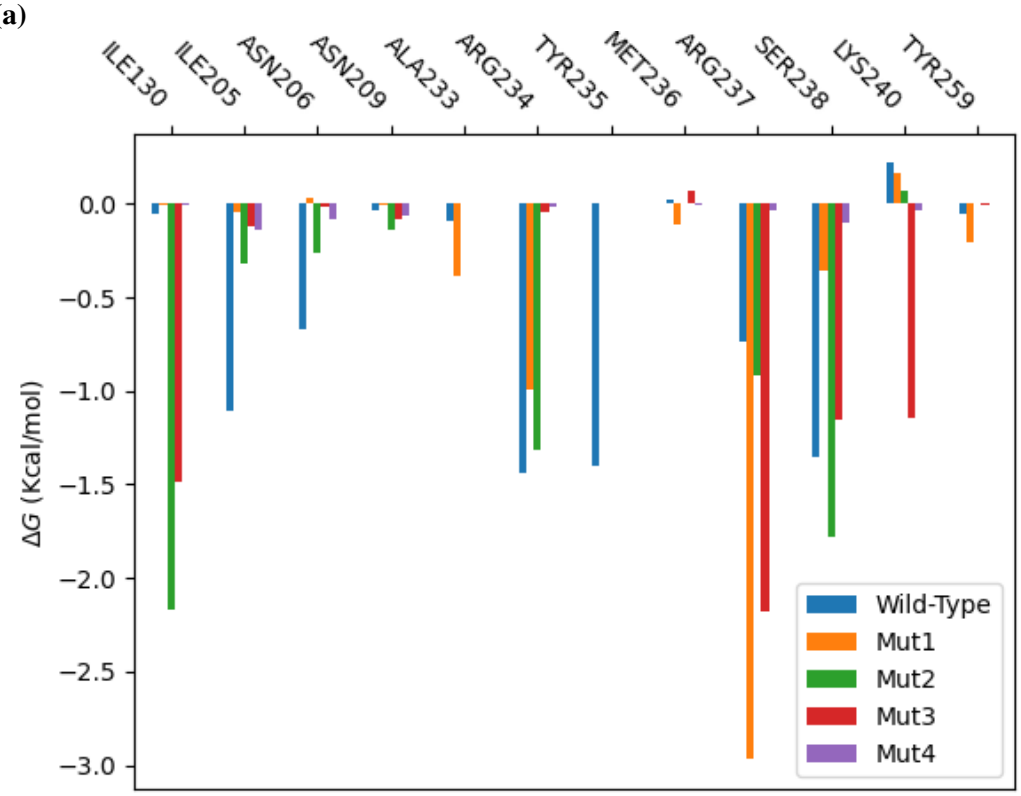

(b)

Figure 5: Energy Decomposition Per-Residues bound to Remdesivir. (a) and (b) are all residue's contributions to the binding affinity.

3.4.4 Contribution Energy Decomposition Per-Residue in Mutants and WT Nsp3-SUD Protein bind to Saquinavir as Inhibitor

In Saquinavir complexes, the energy contribution of decomposition analysis to wild-type and mutant Nsp3-SUD proteins was shown in Figure 6 and Supplementary Table 5. The key residue of PRO35 consistently became a stabilizer, with an extensive effect in mutants 2 and 3. This indicates that certain residues contribute to favourable structural adaptations, enhancing binding affinity by maintaining the optimal conformation of the binding site. The key residues ASP36 and GLN102 decrease the contribution, suggesting destabilization, particularly in mutant 1. It could be caused by side-chain hydrogen bonds or other types of electrostatic interactions. In contrast, the contributions of ILE129 and ILE130 proved mixed stability in mutant complexes. Further, key residues of ARG237 and SER238 show significant destabilization, especially in wild-type, mutants 1, and 4, respectively. The lowest contribution of ARG237 in mutant 1 indicated a loss of stabilizing electrostatic interactions and impaired binding stability. Furthermore, destabilizing contributions of SER238 in mutants 1 and 2 are likely due to structural changes that disturb the protein-ligand interface. In contrast, GLY103, MET236, and TYR235 showed minor impacts on the binding stability, indicating these are not influential residues within Saquinavir binding across the mutants.

Generally, the analysis underlines the impact on the Saquinavir mutation complexes, with key residues PRO35, GLN102, and ARG237 playing a critical role in the stabilization protein-ligand complex. These findings provide fundamental insights into the structural determinants of binding affinity, which are critical in guiding drug design and discovery strategies against SARS-CoV-2.

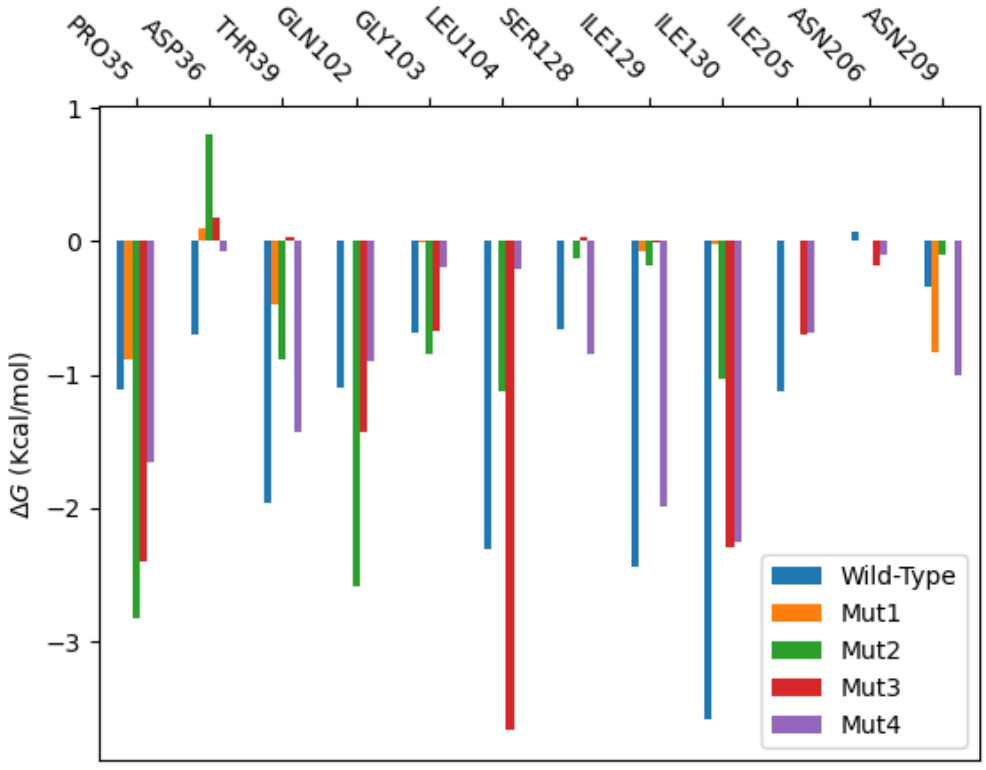

(a)

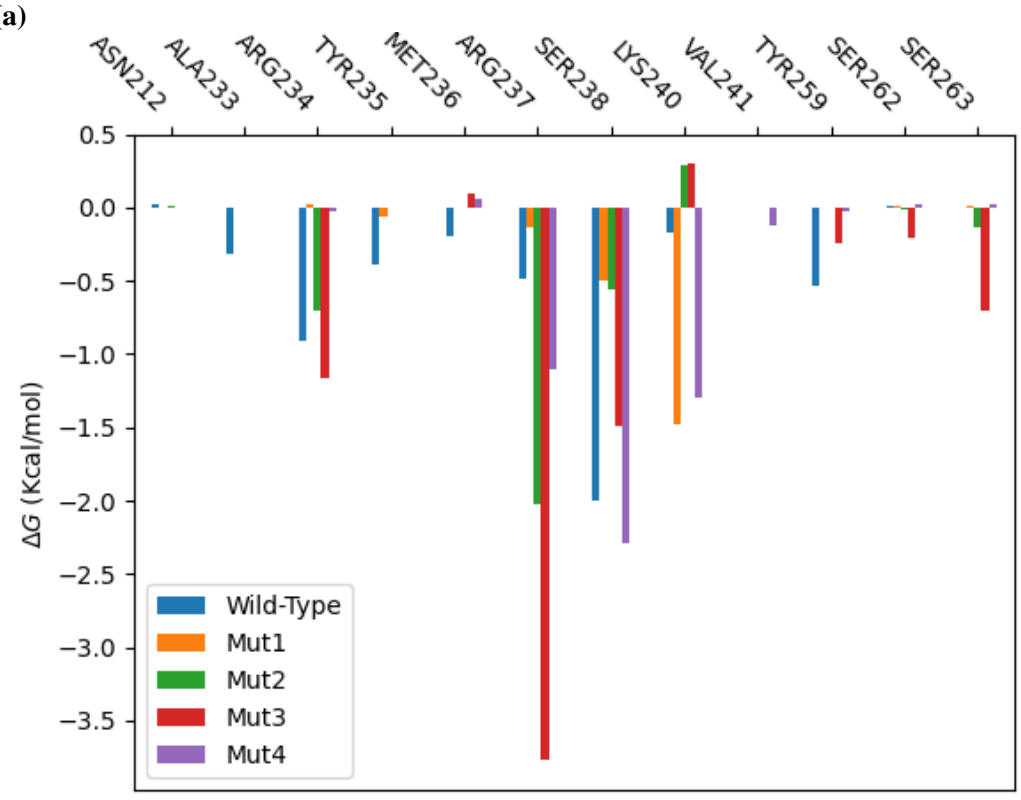

(b)

Figure 6: Energy Decomposition Per-Residues bound to Saquinavir. (a) and (b) are all residue's contributions to the binding affinity.

3.5 Structural flexibility Analysis of Nsp3-SUD complexes with GS-441524 nucleoside core, Remdesivir, and Saquinavir

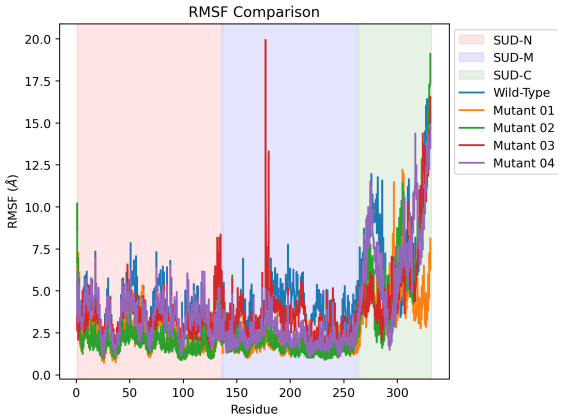

(a) RMSF GS-441524 Complexes.

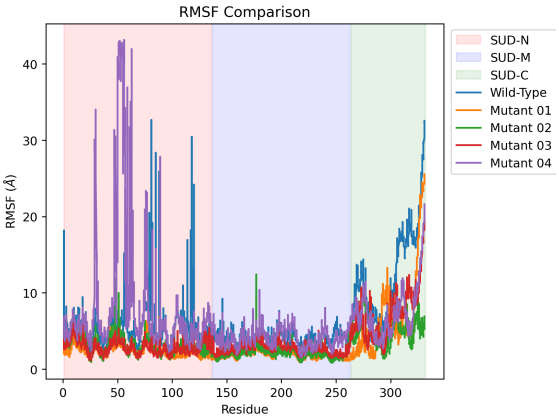

(b) RMSF Remdesivir Complexes.

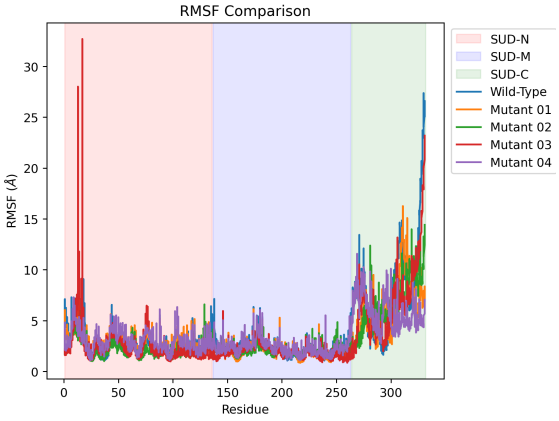

(c) RMSF Saquinavir Complexes.

Figure 7: Comparison RMSF N-M-C (a) GS-441524, (b) Remdesivir, and (c) Saquinavir to wild-type within Mutants 1-3.

The structural flexibility of GS-441524, Remdesivir, and Saquinavir Nsp3-SUD complexes was investigated by applying RMSF analysis (Figure 7). The RMSF profiles revealed a consistent pattern in the N and C-domains, which exhibited higher fluctuations compared to the relatively stable M-domain. Especially mutant 3 showed increased flexibility, with peaks around residues 20-30 in the N-domain of the Saquinavir complex and residues 170-180 in the GS-441524 complex. In both wild-type and mutant complexes, significant fluctuations were observed in the C-domain around residues 264–331, identifying these regions as structural instability hotspots that might contribute to resistance against mutation-induced changes. The increased flexibility in both N and C domains, especially in mutant 3, suggests that mutations could significantly be affected by the consistent fluctuations observed in the C-domain around residues 264-331. These findings underline the sensitivity of the N and C domains to mutations and their potential as targets for stabilizing interventions.

However, the robust stability of the M-domain might indicate that it acts as a scaffold for structural stability even in the presence of mutations. These findings are important concerning future

drug design and discovery strategies, especially for optimizing binding affinity and mitigating destabilization by mutations in Nsp3-SUD complexes.

3.6 Comparison of Key Residues Binding Interactions and Effects of Mutations in wild-type and mutant Nsp3-SUD complexes

The binding interactions between Nsp3-SUD and the potential ligands GS-441524, Remdesisvir, and Saquinavir were analyzed to identify how mutations influence the stability of the protein-ligand complex. The analysis focused on hydrophobic, van der Waals (vdW), hydrogen bonding (HBDonor), and π-cation interactions, each contributing differently to binding stability depending on the ligand and mutation. (Supplementary Tables 6, 7, 8, Supplementary Figures 12-41).

The mutations increase the ligand interaction through ASP36 dominant in all mutants. The highest interactions, especially in mutants 1, 2, and 4, contributed to HBDonor and vdW contact from 99.40% to 100%. However, mutant 3 showed a change from 62.93% to 63.73%. ARG237 emerges as a critical stabilizer while providing hydrophobic, π-cation, and vdW interactions, the pinpoint in mutant 1 with 92.40% π-cation and mutant 4 with 93.50% hydrophobic interaction. Furthermore, mutated residue T266I contributed with 36.86% vdW interactions in the wild-type. However, its contribution interactions disappeared in all mutants. This indicates that the structural adjustment was driven by the increased involvement of the other residues.

In Remdesivir complexes, the hydrophobic contribution of PRO35 is especially high in mutant 1, with a contribution of 99.60% and 64.63% vdW contact. These interactions keep the ligand oriented and stable in the binding pocket. However, these interactions are absent in mutants 2 and 4, causing the lower complex stability. It revealed the fundamental role of PRO35 in protein-ligand stability by allowing close contact between the ligand and the protein. In addition, ASP36, GLN102, and ARG237 are also highly contributing to vdW contact, HB donor, and hydrophobic interactions in several mutants. Mutants 2 and 3 exhibited vdW contact from 35.06% to 42.82% and 53.24 to 67.79%, respectively. Especially in mutant 1, the highest vdW interaction is 77.62%, further supporting the binding affinity of non-covalent interactions. The highlight of impaired effects on stability was observed in mutant 4.

In Saquinavir complexes, the key residue PRO35 predominantly engages in hydrophobic and van der Waals interactions in both wild-type and mutant forms. The highest interactions were observed in wild-type, followed by mutants 2 and 4, respectively. The hydrophobic interactions between Saquinavir and key residue GLN102 in mutants 2, 3, and 4 (from 52.93% to 65.38%) suggest that Saquinavir plays a crucial role in stabilizing the complex. However, mutant 1 was revealed to disrupt these hydrophobic interactions, leading to reduced binding affinity. Hydrogen bonding interactions also play a critical role in stabilizing the protein-ligand interactions, especially ASP36 in mutant 3. The structural integrity of the binding site contributes about 45.65% to 60.83%. This highlights that HBDonor interaction could enhance the binding protein-ligand by enhancing favourable electrostatic interactions. However, disrupted interactions could reduce the binding stability, as observed in the wild-type, mutants 1, 2, and 4 complexes. Additionally, π-cation interactions are essential for complex stabilization in the presence of aromatic residues. ARG237 contributes significantly to π-cation interactions, particularly in mutant 2 (31.92%). Furthermore, hydrogen bonding, hydrophobic forces, and van der Waals interactions collectively contribute to the stabilization of mutants 2, 3, and 4. Moreover, GLY103 contributes to vdW contact and hydrogen bond in mutant 2 (85.49% and 59.29%), stabilizing the ligand-binding interactions. The fundamental type of interaction, including hydrophobic, vdW, HB donor, and π-cation, has played a role in stabilizing protein-ligand complexes. The key residues are PRO35, GLN102,

ASP36, ARG237, and GLY103, which suggest stability interactions. The highlights provide insights for drug design and discovery to optimize ligand affinity and stability.

4 Conclusions

This study investigates the impact of Indonesian-specific mutations in the Nsp3-SUD on drug binding stability using molecular dynamics and end-point energy calculations (MM/PBSA and MM/GBSA). Mutations A76S-G77S-T266I, A76S, G77S-K175R, and D302G were identified using a covariance-based MAAFT algorithm for multiple sequence alignment (MSA) and further validated by structural homology modeling. The ΔG and $\Delta\Delta G$ analyses revealed mutation-specific effects on ligand binding and drug resistance potential. Mutant 1 stabilized the binding of GS-441524 and Remdesivir, suggesting promising efficacy against these mutants. Mutant 3 exhibited moderate stability, particularly with Remdesivir and Saquinavir, making them potential candidates for therapy. Meanwhile, Mutant 4 demonstrated strong binding with GS-441524 and Saquinavir, indicating promising drug efficacy; however, the interaction with Remdesivir raised concerns regarding the potential of resistance mechanisms. Mutant 2 showed a high binding affinity with all drug candidates while maintaining moderate binding stability. Structured analysis revealed that the mutations increased flexibility in the N and C domains, whereas the M domain remained stable. The structural analysis identified PRO35, GLN102, and ARG237 as key amino acid residues that significantly contribute to binding stabilization. These results also highlight the importance of mutation effects on drug binding and the fundamental design of antiviral therapies against mutants of SARS-CoV-2. This study has provided critical mechanistic insights into the structural determinants for binding affinity toward drug-design optimization and increased efficacy in therapeutic strategies targeting SARS-CoV-2 variants.

5 Acknowledgments

This work was supported by JSPS KAKENHI Grant Numbers 23K03339 (K.K) and 23K03338 (H.N), as well as HaKaSe^{+} for SPRING of Kanazawa University. We also gratefully acknowledge the use of supercomputing resources provided by the Research Center for Computational Science (RCCS).

Supplementary

A Molecular Dynamics Analysis

A.1 Root Mean Square Deviation (RMSD)

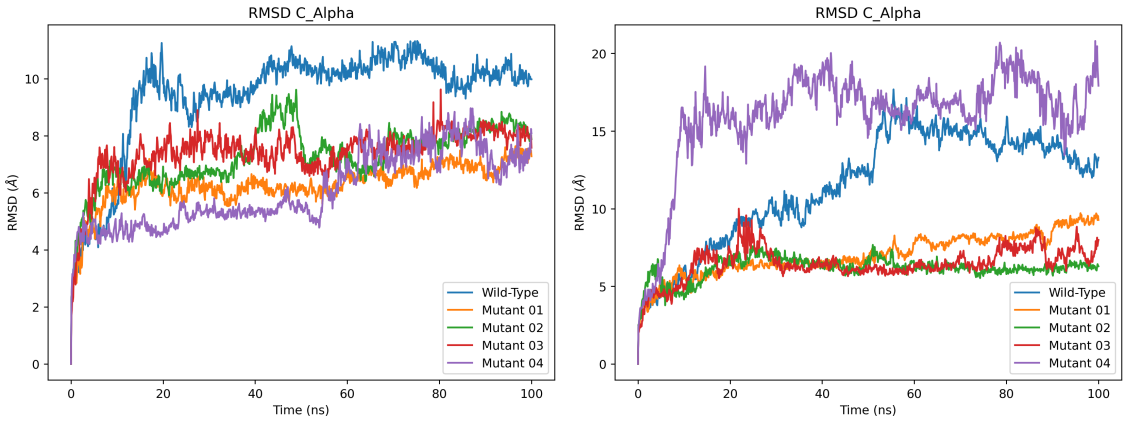

(a) GS-441524.

(b) Remdesivir.

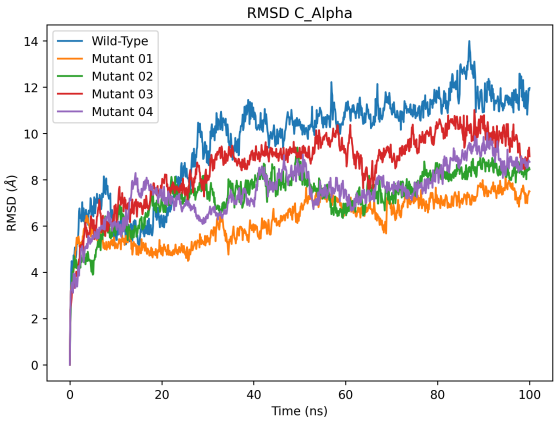

(c) Saquinavir.

Figure 8: Comparison RMSD N-M-C (a) GS-441524, (b) Remdesivir, and (c) Saquinavir to wild-type within Mutants 1-4.

A.2 SASA (Solvent Accessible Surface Area)

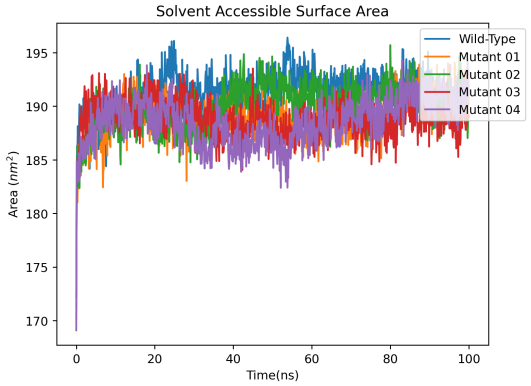

(a) GS-441524 to Mutants 1-4 SUD.

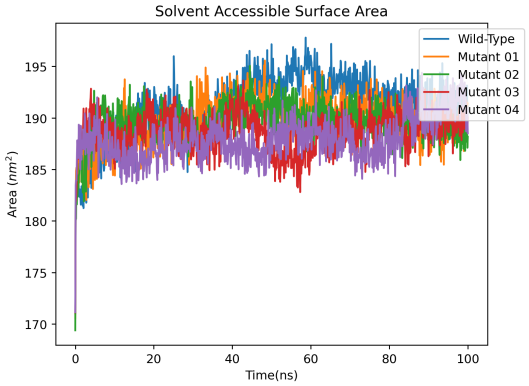

(b) Remdesivir to Mutants 1-4 SUD.

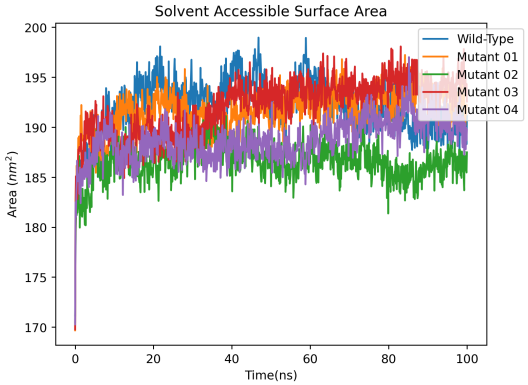

(c) Saquinavir to Mutants 1-4 SUD.

Figure 9: Comparison SASA of (a) GS-441524, (b) Remdesivir, and (c) Saquinavir to wild-type within Mutants 1-4.

A.3 Radius of Gyration

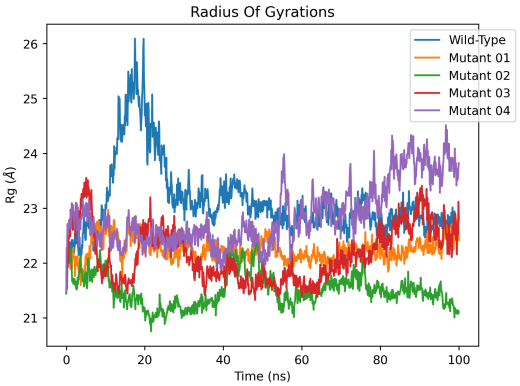

(a) GS-441524 to Mutants 1-4 SUD.

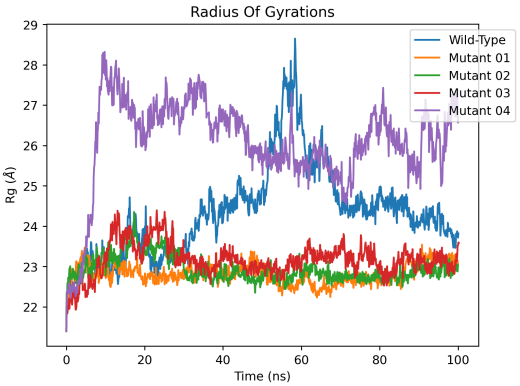

(b) Remdesivir to Mutants 1-4 SUD.

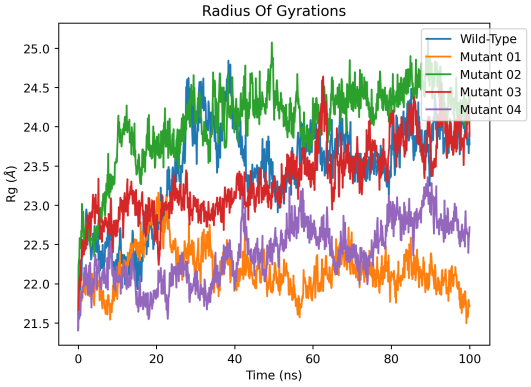

(c) Saquinavir to Mutants 1-4 SUD.

Figure 10: Comparison of the Radius of gyration of (a) GS-441524, (b) Remdesivir, and (c) Saquinavir to wild-type within Mutants 1-4.

A.4 Hydrogen Bond

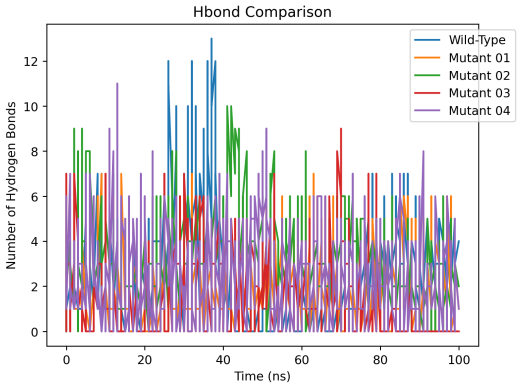

(a) GS-441524 to Mutants 1-4 SUD.

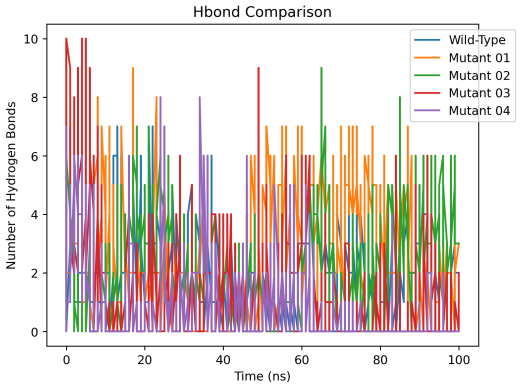

(b) Remdesivir to Mutants 1-4 SUD.

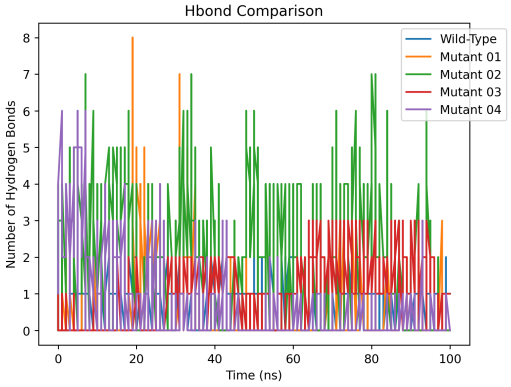

(c) Saquinavir to Mutants 1-4 SUD.

Figure 11: Comparison Hydrogen Bonds of (a) GS-441524, (b) Remdesivir, and (c) Saquinavir to wild-type within Mutants 1–4.

B Fingerprint Interaction types per-residues contribution in the binding affinity complexes to ligands

B.1 Fingerprint Interaction types per-residues contribution in the binding affinity of wild-type complexes to ligands

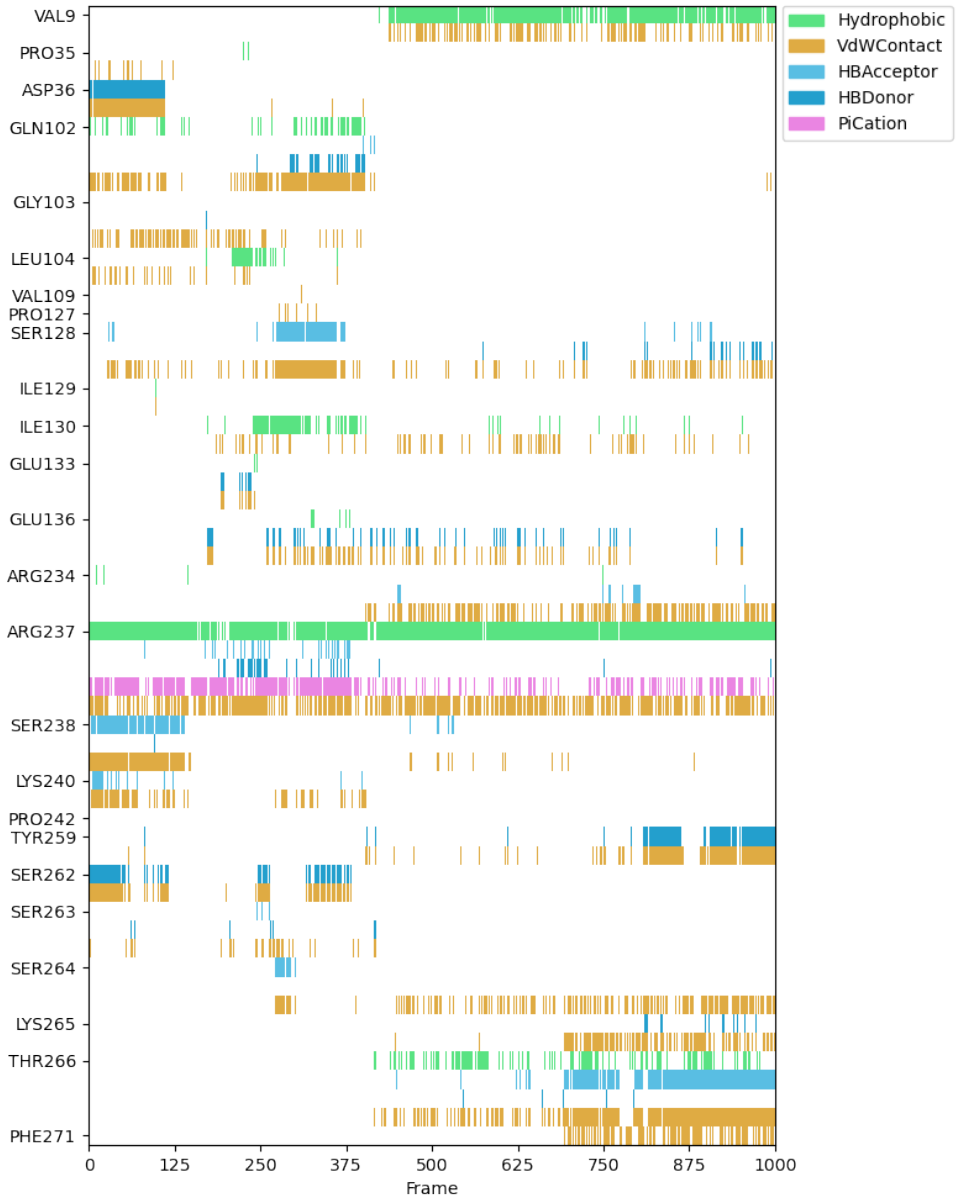

Figure 12: Binding interaction Per-Residue of the studied Nsp3-SUD wild-type to GS-441524 Nucleoside core.

Figure 13: Binding interaction Per-Residue of the studied Nsp3-SUD wild-type to Remdesivir.

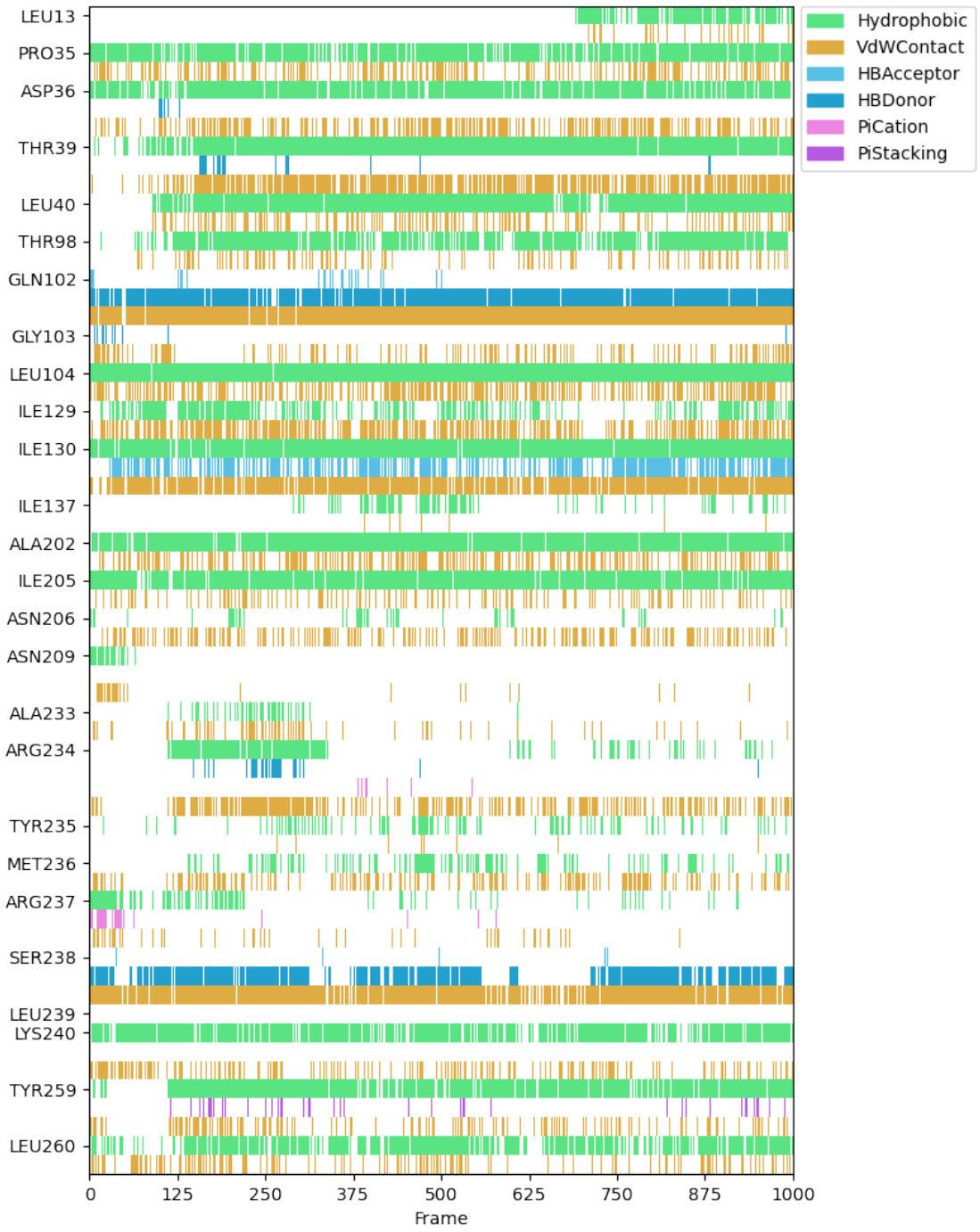

Figure 14: Binding interaction Per-Residue of the studied Nsp3-SUD wild-type to Saquinavir.

B.2 Fingerprint Interaction types per-residues contribution in the binding affinity of Mutant 1 complexes to ligands

Figure 15: Binding interaction Per-Residue of the studied Nsp3-SUD Mutated 1 to GS-441524 Nucleoside core.

Figure 16: Binding interaction Per-Residue of the studied Nsp3-SUD Mutated 1 to Remdesivir.

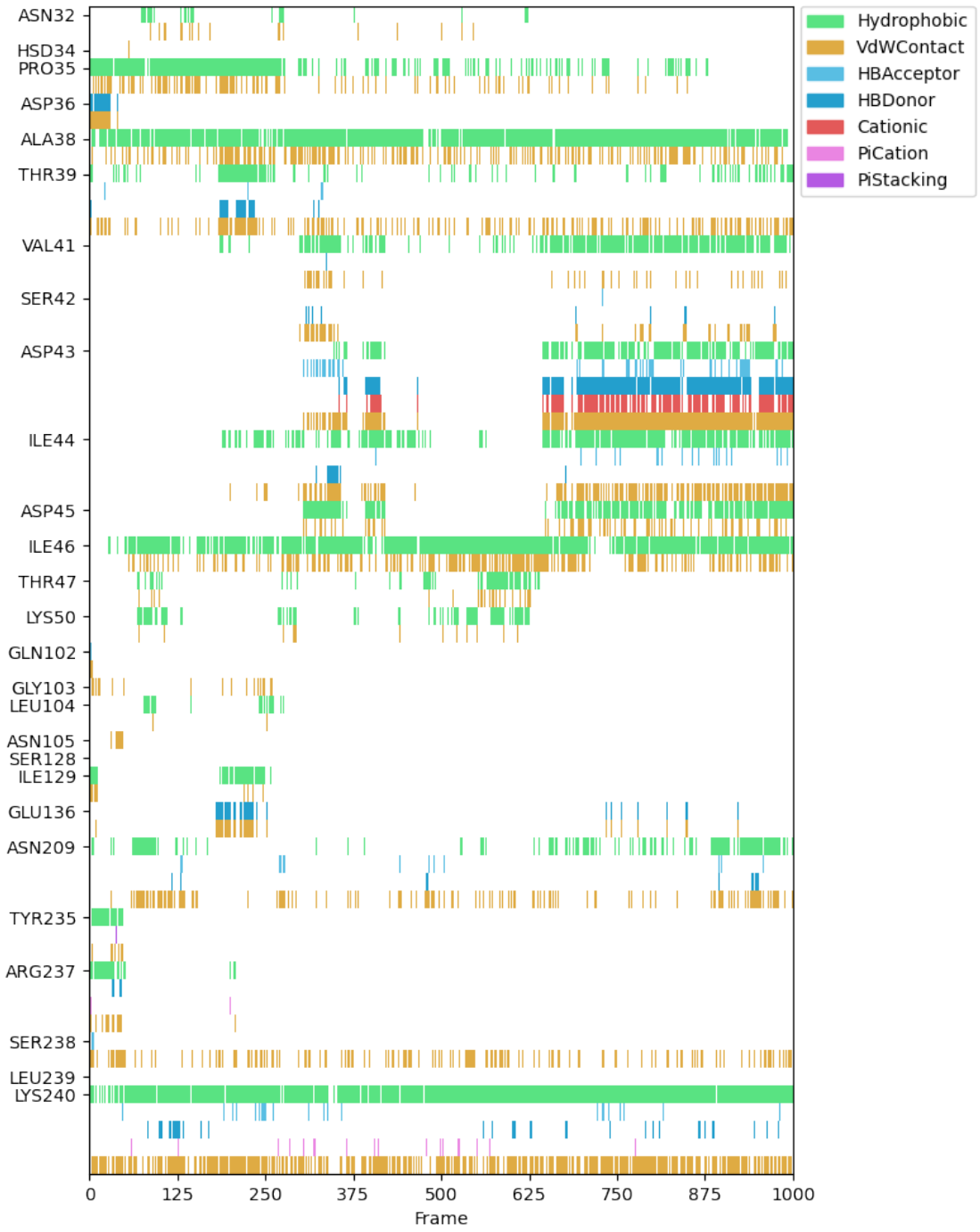

Figure 17: Binding interaction Per-Residue of the studied Nsp3-SUD Mutated 1 to Saquinavir.

B.3 Fingerprint Interaction types per-residues contribution in the binding affinity of Mutant 2 complexes to ligands

Figure 18: Binding interaction Per-Residue of the studied Nsp3-SUD Mutated 2 to GS-441524 Nucleoside core.

Figure 19: Binding interaction Per-Residue of the studied Nsp3-SUD Mutated 2 to Remdesivir.

Figure 20: Binding interaction Per-Residue of the studied Nsp3-SUD Mutated 2 to Saquinavir.

B.4 Fingerprint Interaction types per-residues contribution in the binding affinity of Mutant 3 complexes to ligands

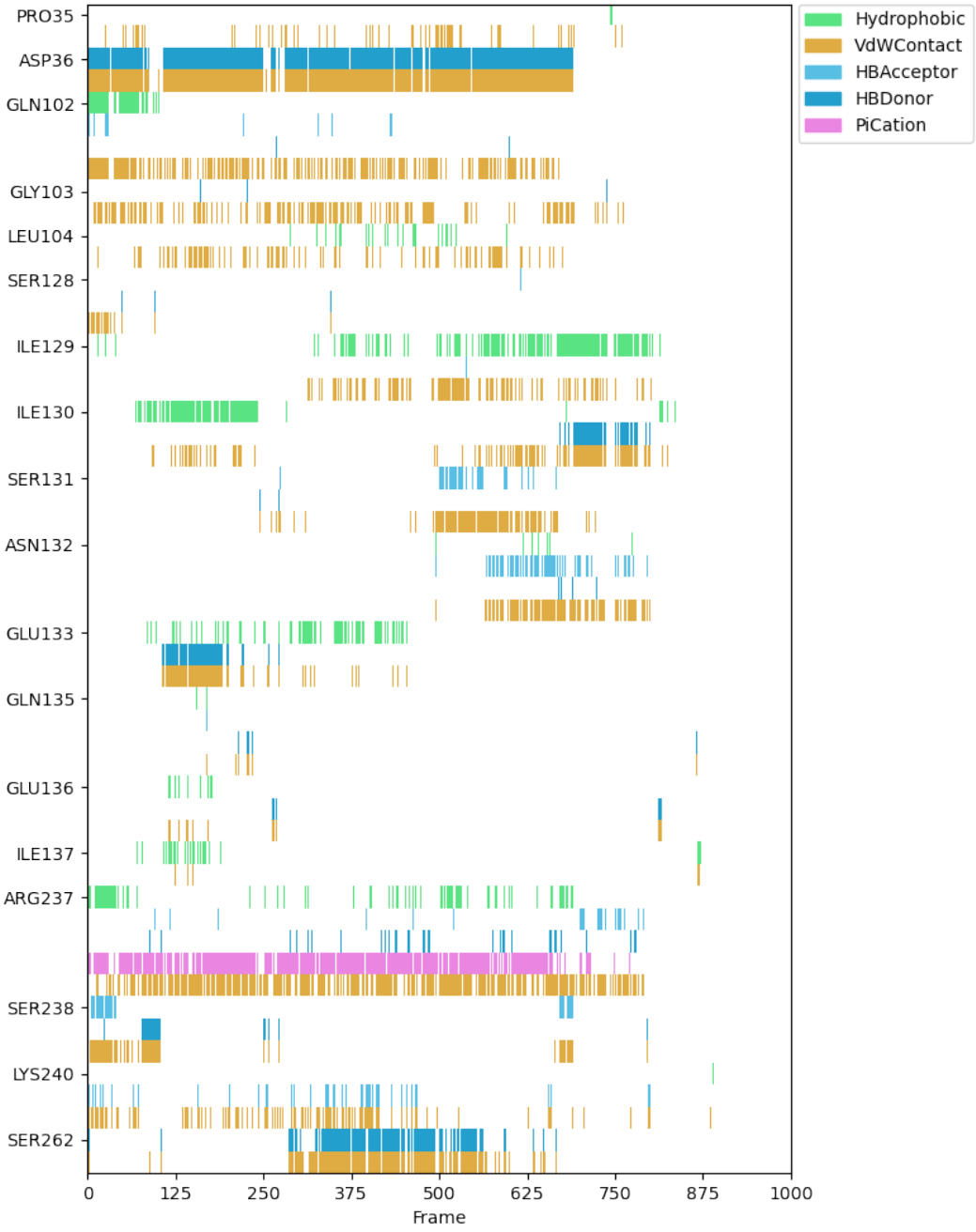

Figure 21: Binding interaction Per-Residue of the studied Nsp3-SUD Mutated 3 to GS-441524 Nucleoside core.

Figure 22: Binding interaction Per-Residue of the studied Nsp3-SUD Mutated 3 to Remdesivir.

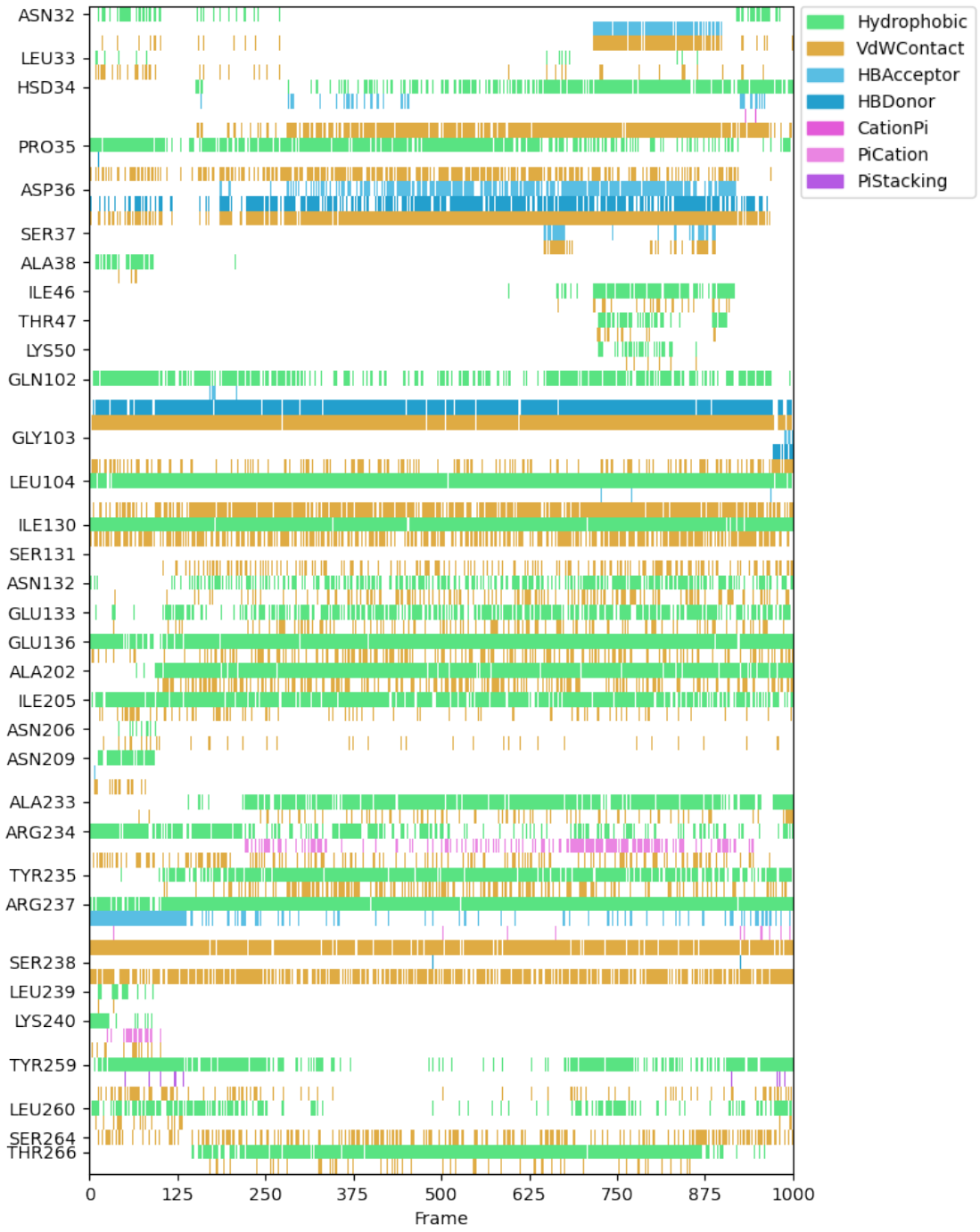

Figure 23: Binding interaction Per-Residue of the studied Nsp3-SUD Mutated 3 to Saquinavir.

B.5 Fingerprint Interaction types per-residues contribution in the binding affinity of Mutant 4 complexes to ligands

Figure 24: Binding interaction Per-Residue of the studied Nsp3-SUD Mutated 4 to GS-441524 Nucleoside core.

Figure 25: Binding interaction Per-Residue of the studied Nsp3-SUD Mutated 4 to Remdesivir.

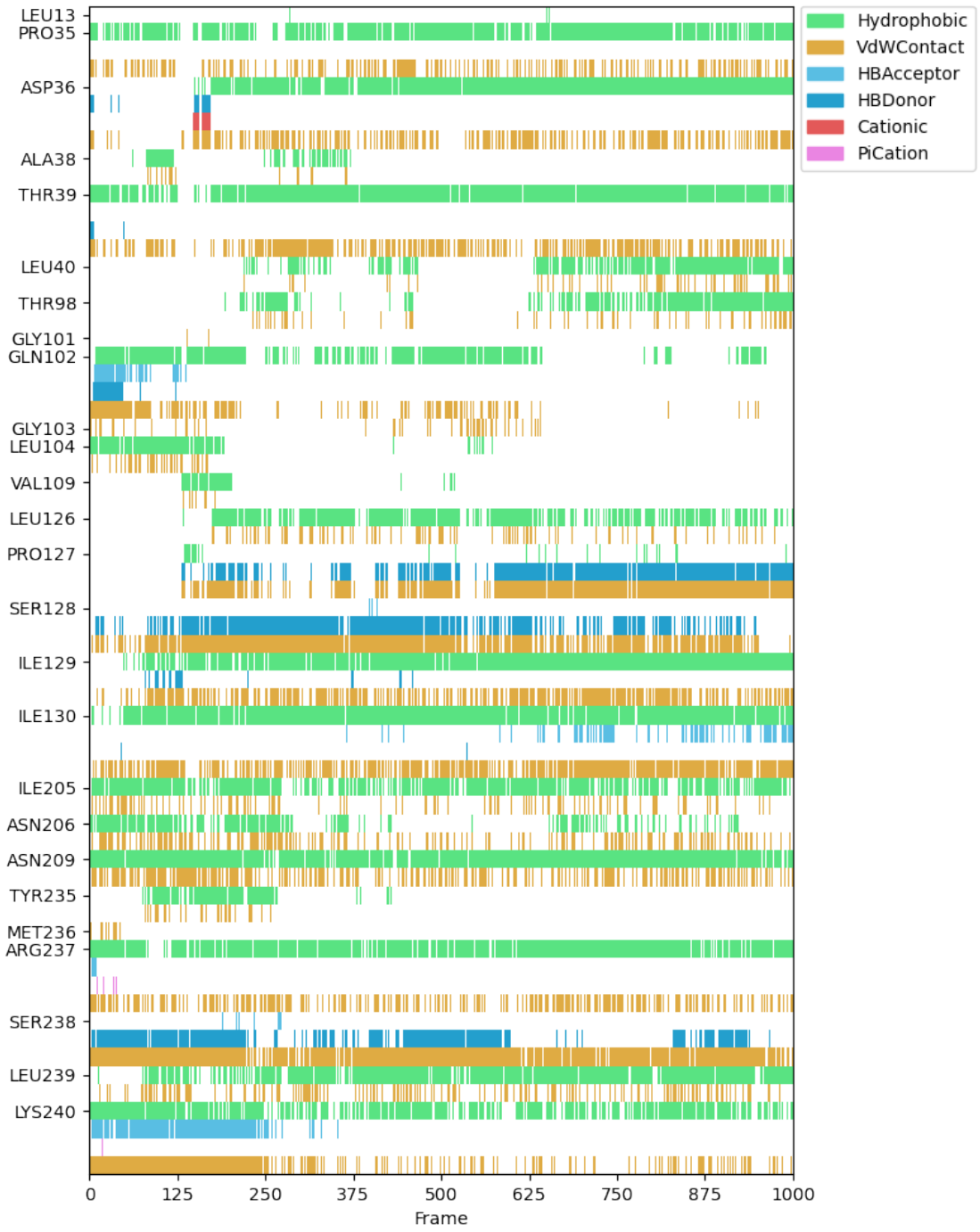

Figure 26: Binding interaction Per-Residue of the studied Nsp3-SUD Mutated 4 to Saquinavir.

C Comparison of Protein-Ligand Interaction Nsp3-SUD Complexes

C.1 Comparison 2D Interaction Key Residue in Wild-type Complexes

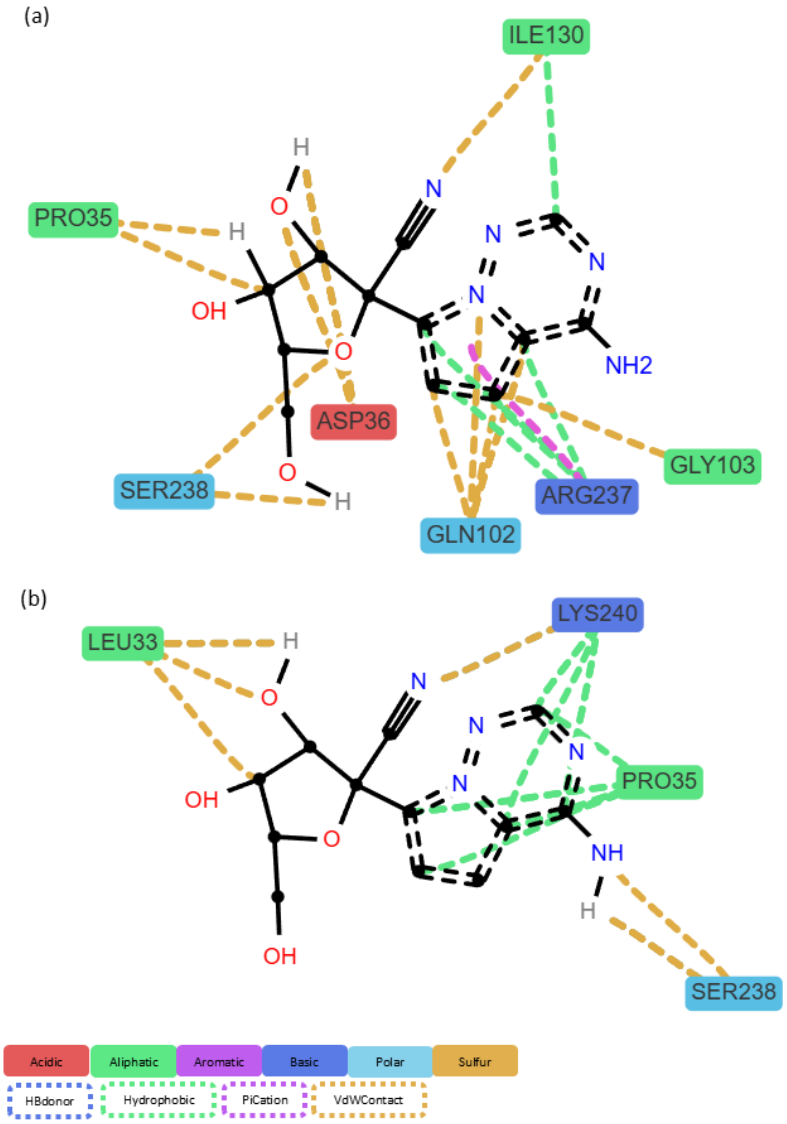

Figure 27: Interactions with residues in the WT complex GS-441524 during frame 0 (a) and frame 1000 (b), respectively.

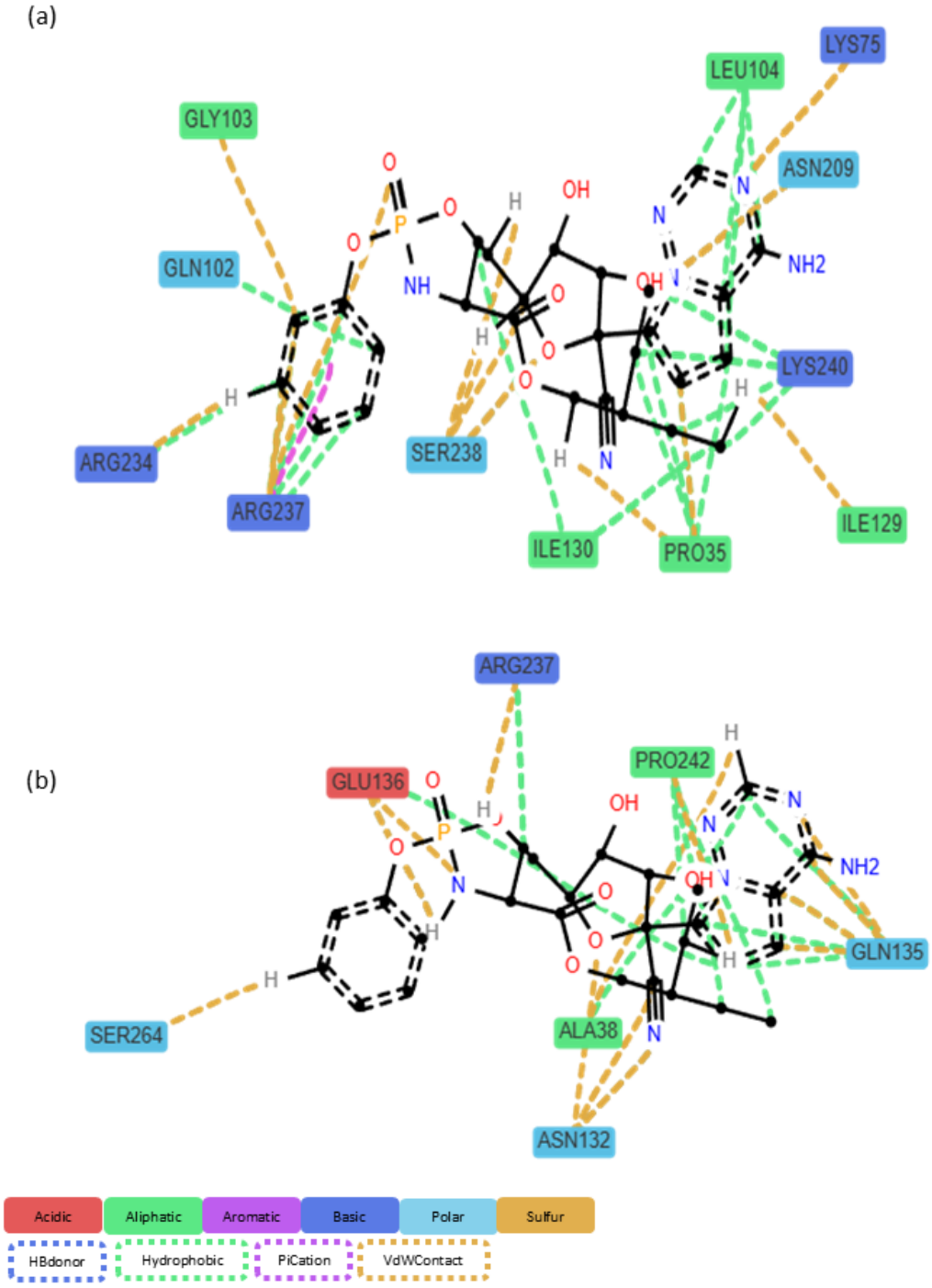

Figure 28: Interactions with residues in the WT complex Remdesivir during frame 0 (a) and frame 1000 (b), respectively.

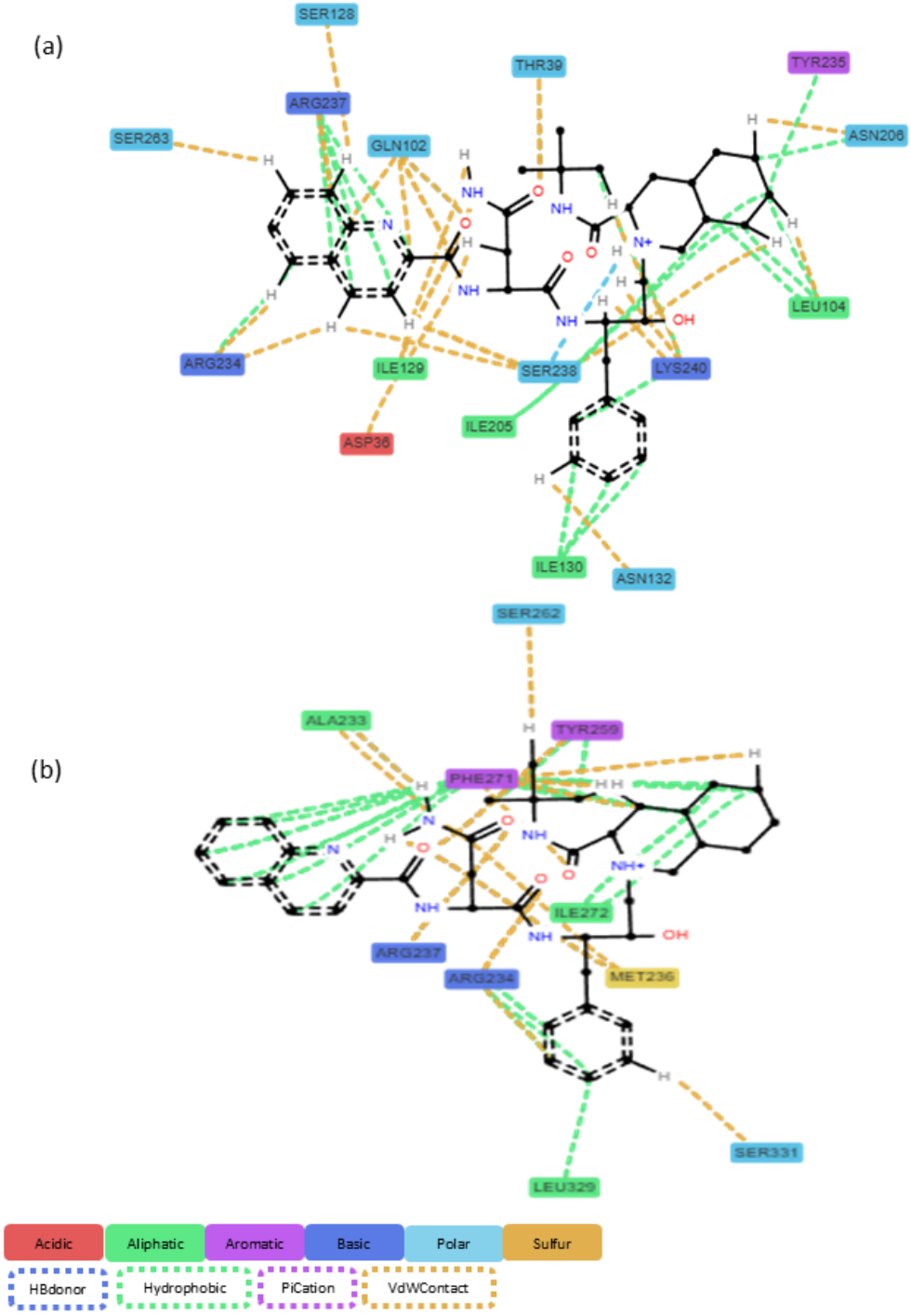

Figure 29: Interactions with residues in the WT complex Saquinavir during frame 0 (a) and frame 1000 (b), respectively.

C.2 Comparison 2D Interaction Key Residue in Mutant 1 Complexes

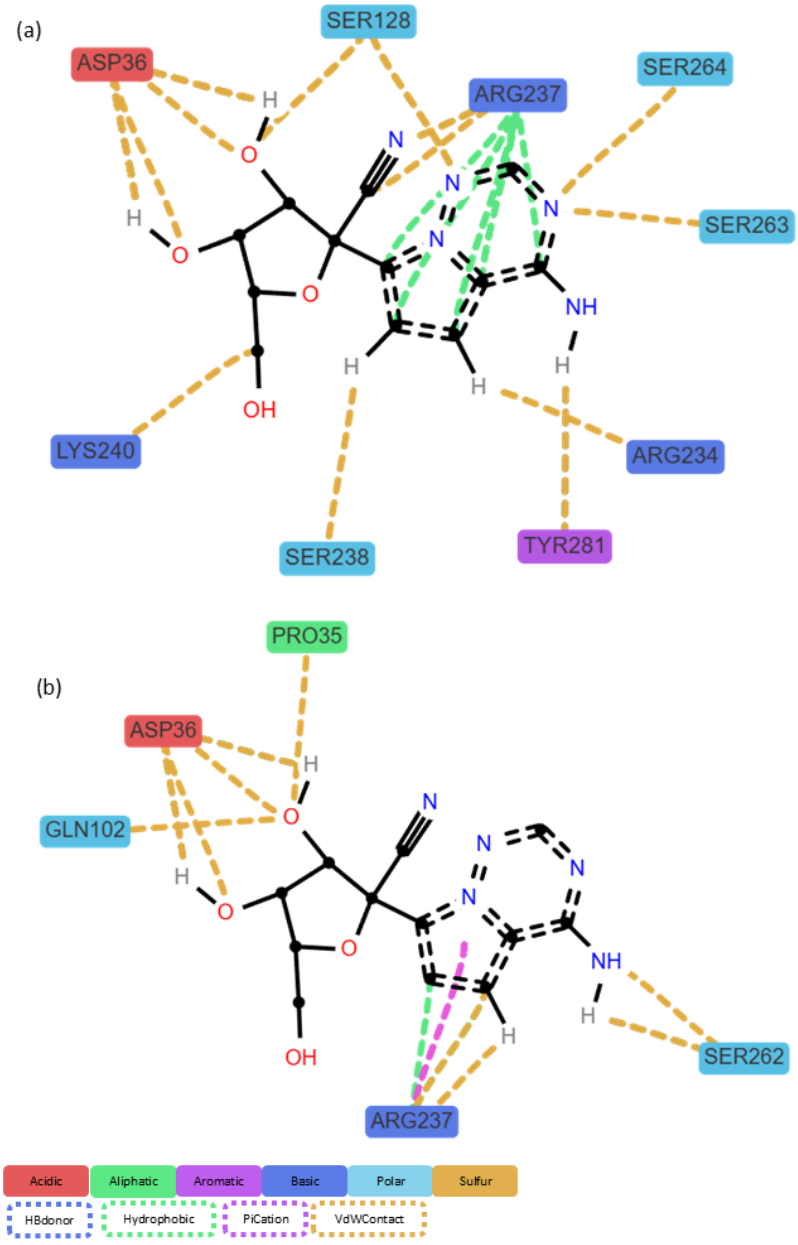

Figure 30: Interactions with residues in the Mutant 1 complex GS-441524 during frame 0 (a) and frame 1000 (b), respectively.

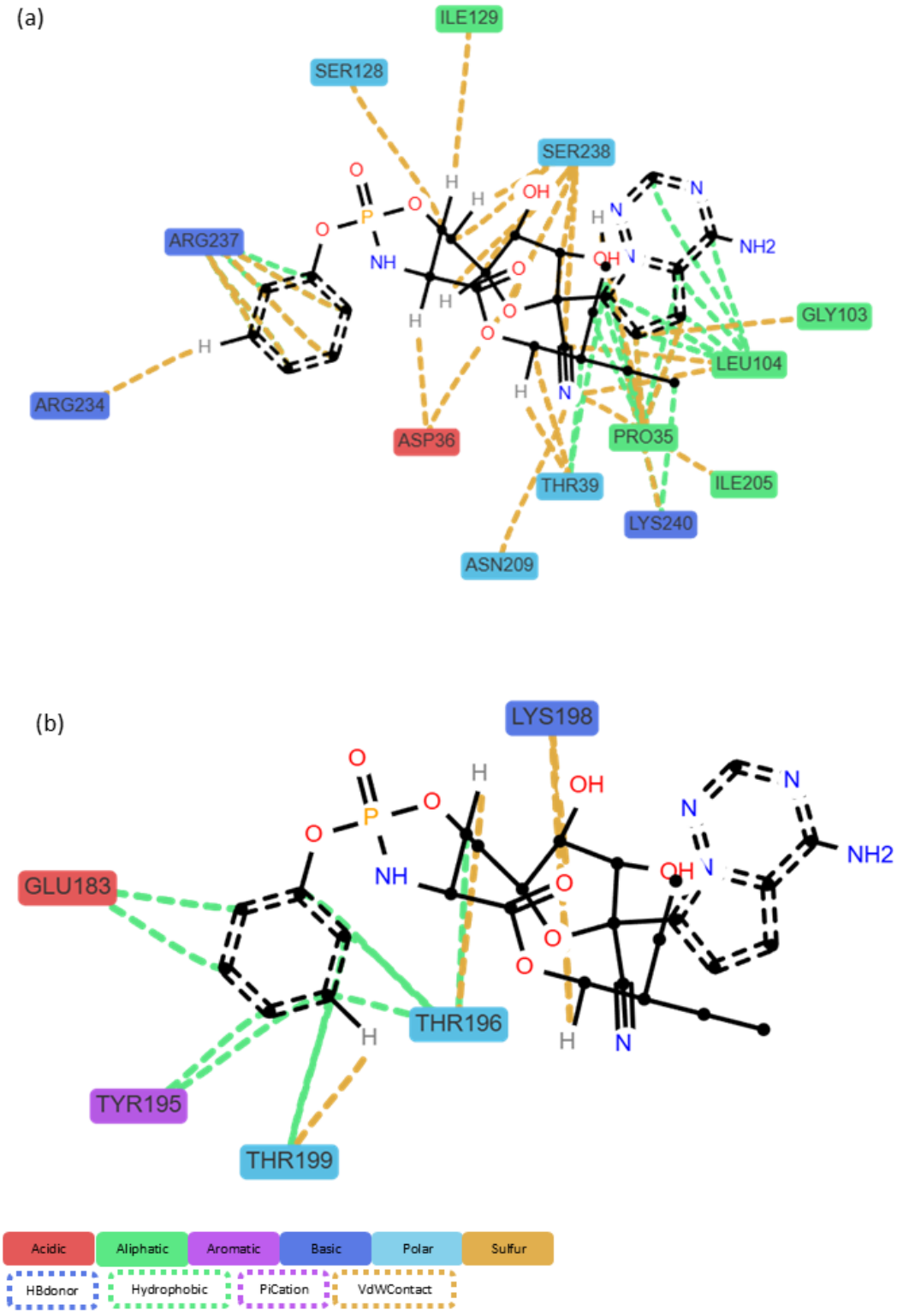

Figure 31: Interactions with residues in the Mutant 1 complex Remdesivir during frame 0 (a) and frame 1000 (b), respectively.

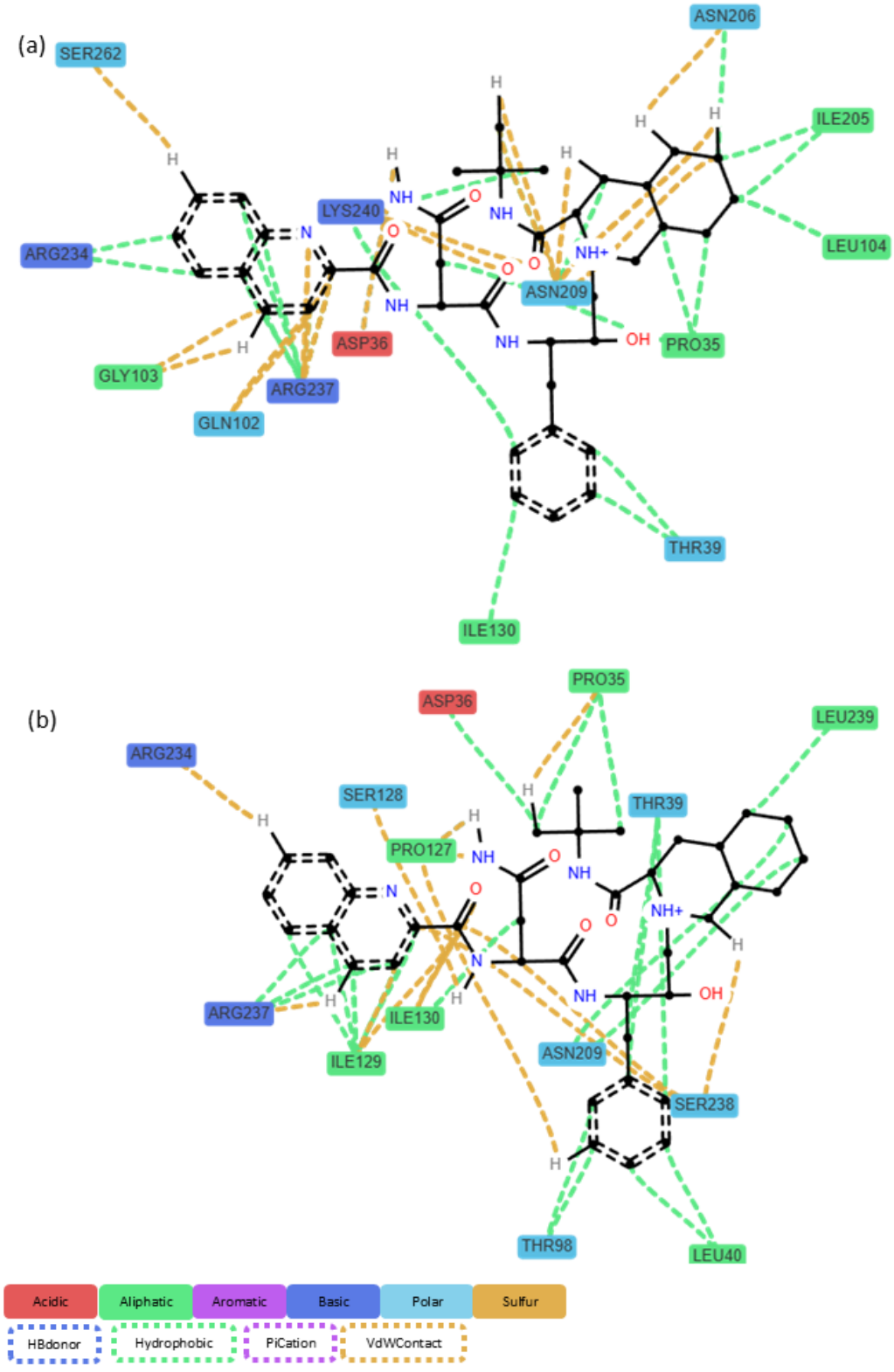

Figure 32: Interactions with residues in the Mutant 1 complex Saquinavir during frame 0 (a) and frame 1000 (b), respectively.

C.3 Comparison 2D Interaction Key Residue in Mutant 2 Complexes

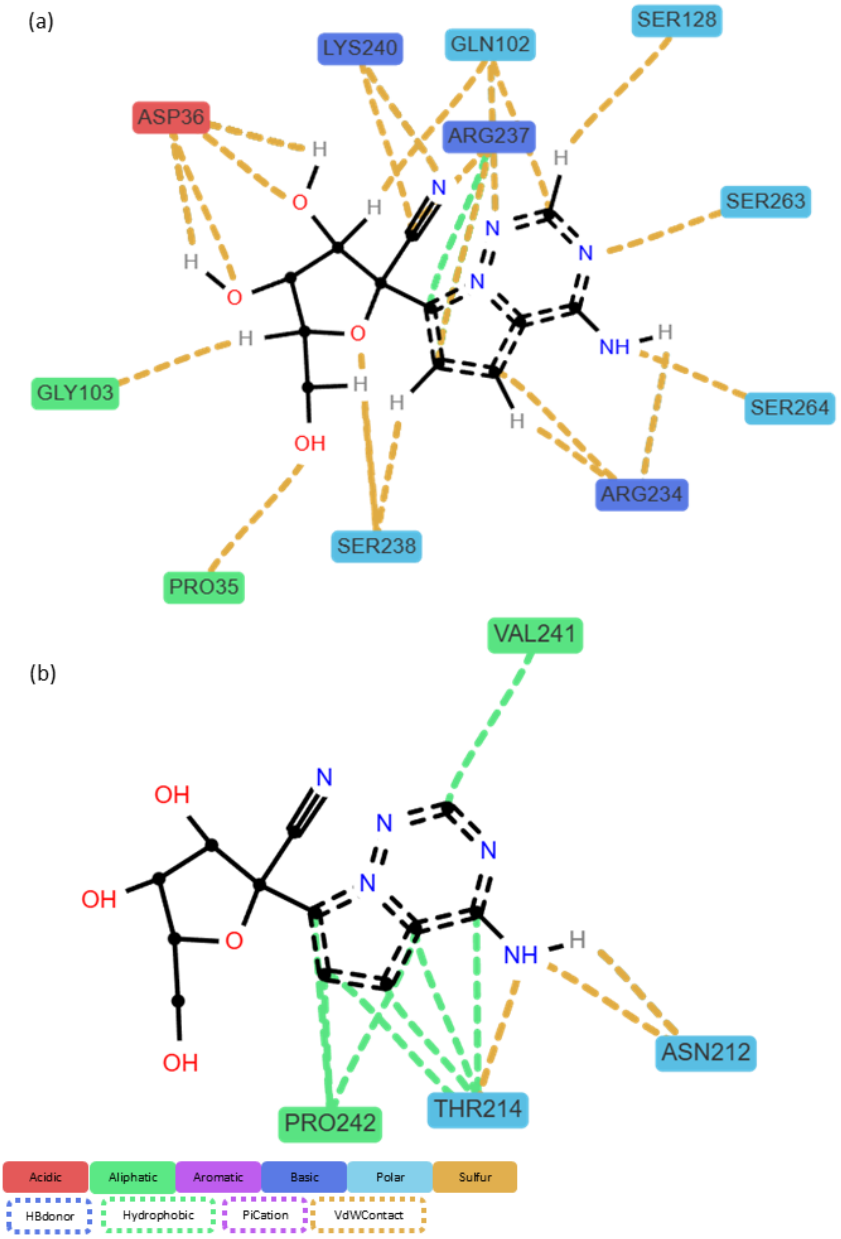

Figure 33: Interactions with residues in the Mutant 2 complex GS-441524 during frame 0 (a) and frame 1000 (b), respectively.

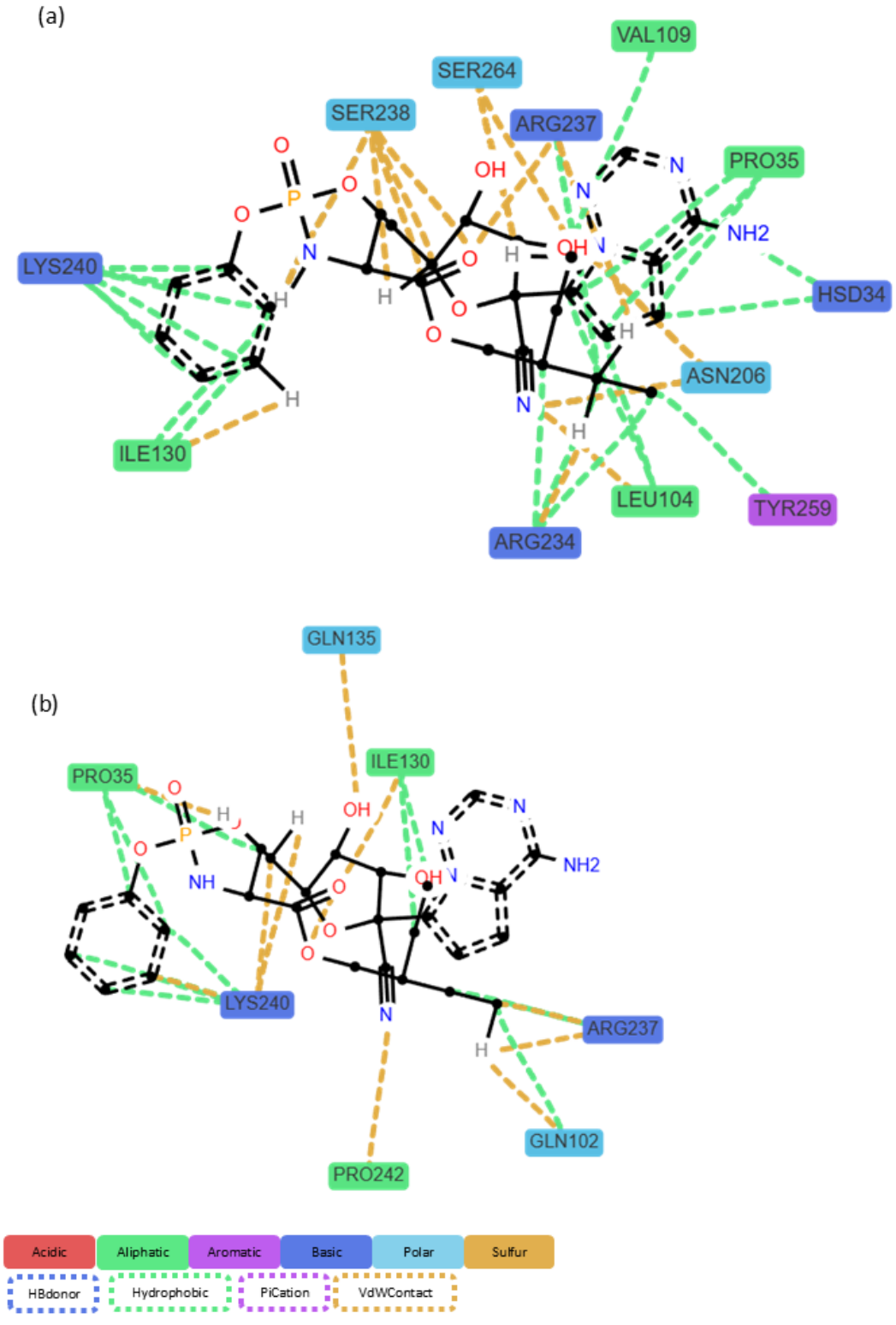

Figure 34: Interactions with residues in the Mutant 2 complex Remdesivir during frame 0 (a) and frame 1000 (b), respectively.

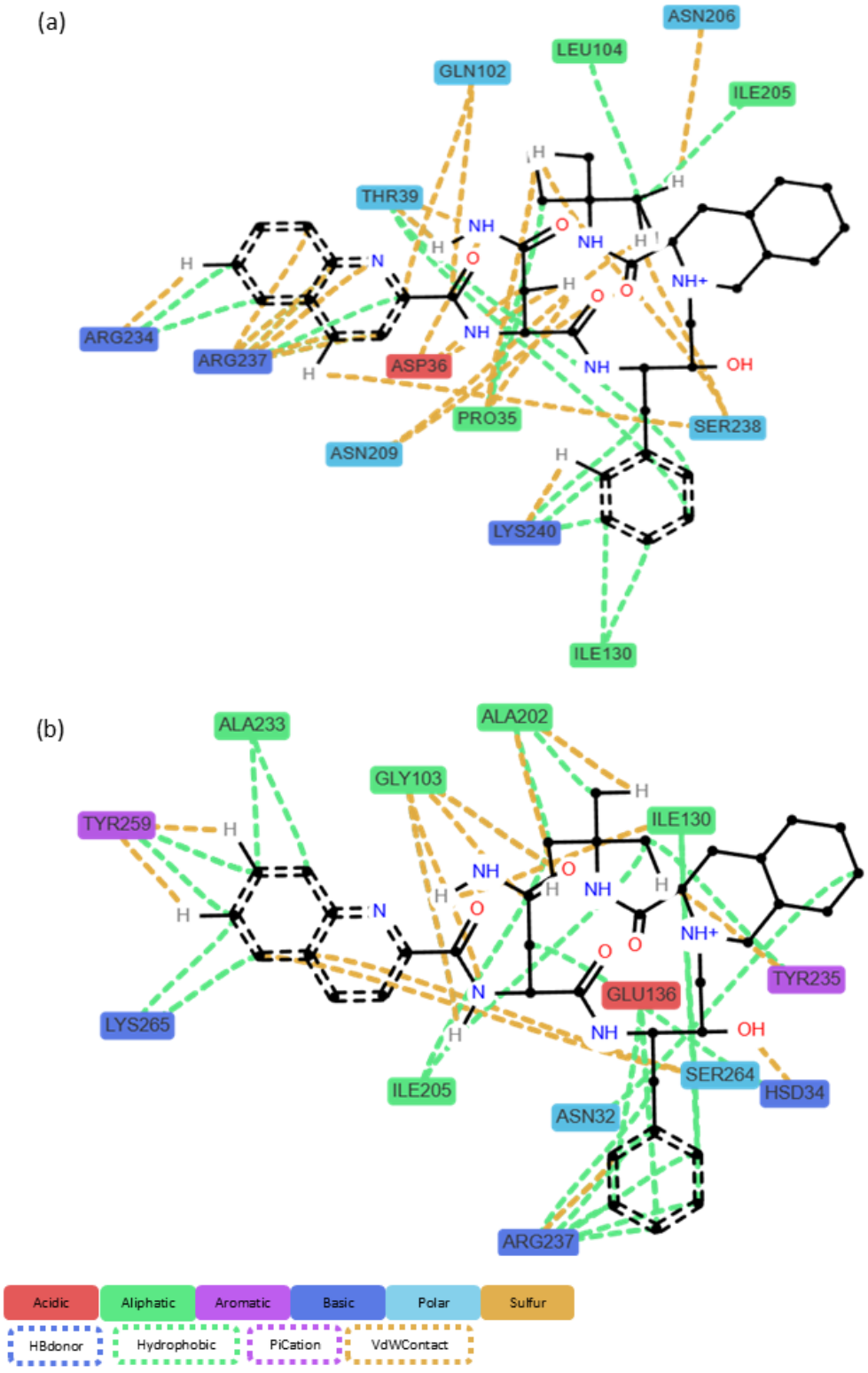

Figure 35: Interactions with residues in the Mutant 2 complex Saquinavir during frame 0 (a) and frame 1000 (b), respectively.

C.4 Comparison 2D Interaction Key Residue in Mutant 3 Complexes

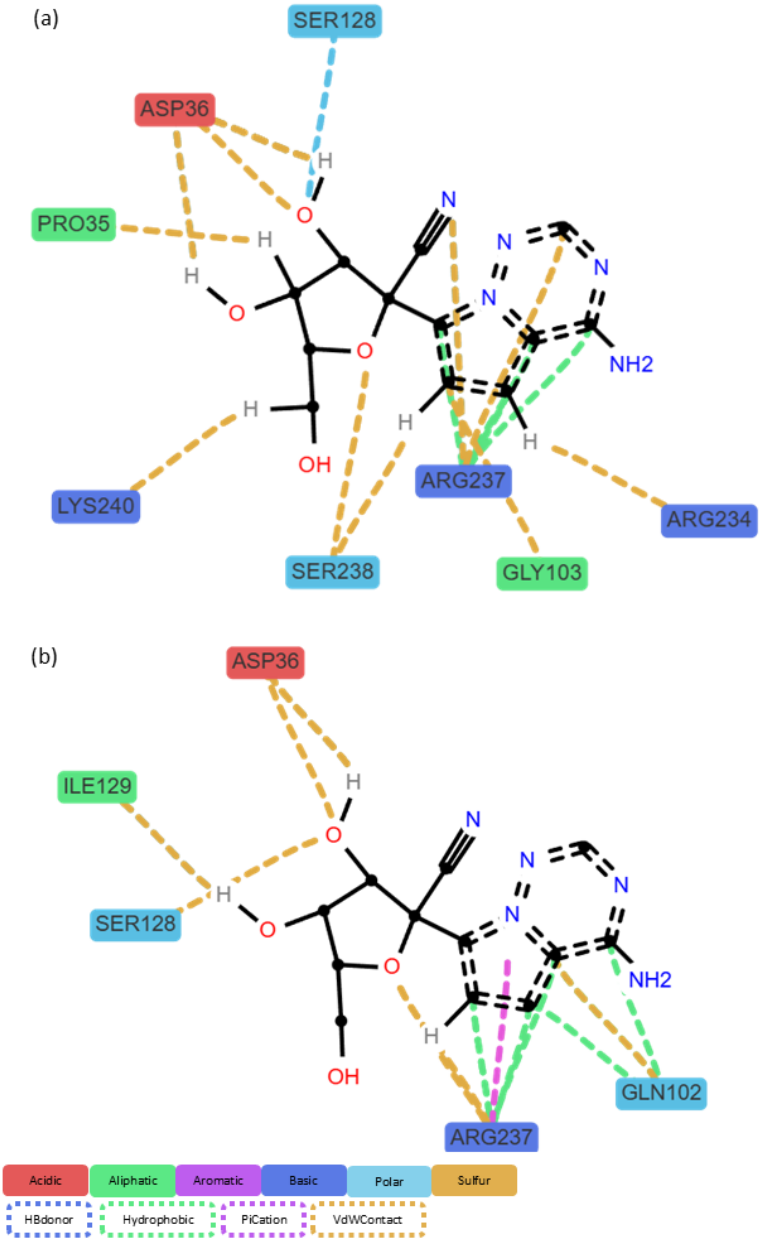

Figure 36: Interactions with residues in the Mutant 3 complex GS-441524 during frame 0 (a) and frame 1000 (b), respectively.

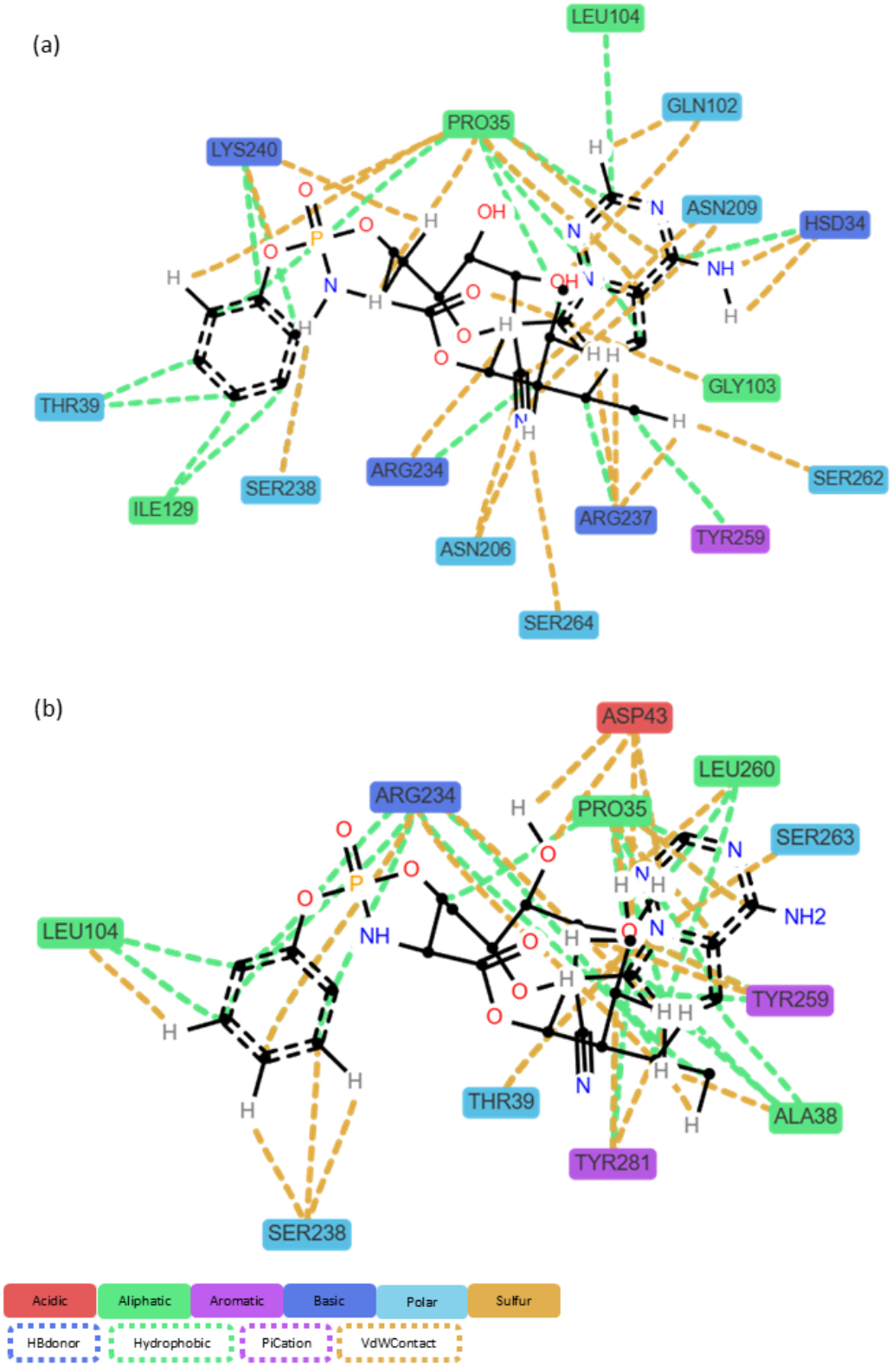

Figure 37: Interactions with residues in the Mutant 3 complex Remdesivir during frame 0 (a) and frame 1000 (b), respectively.

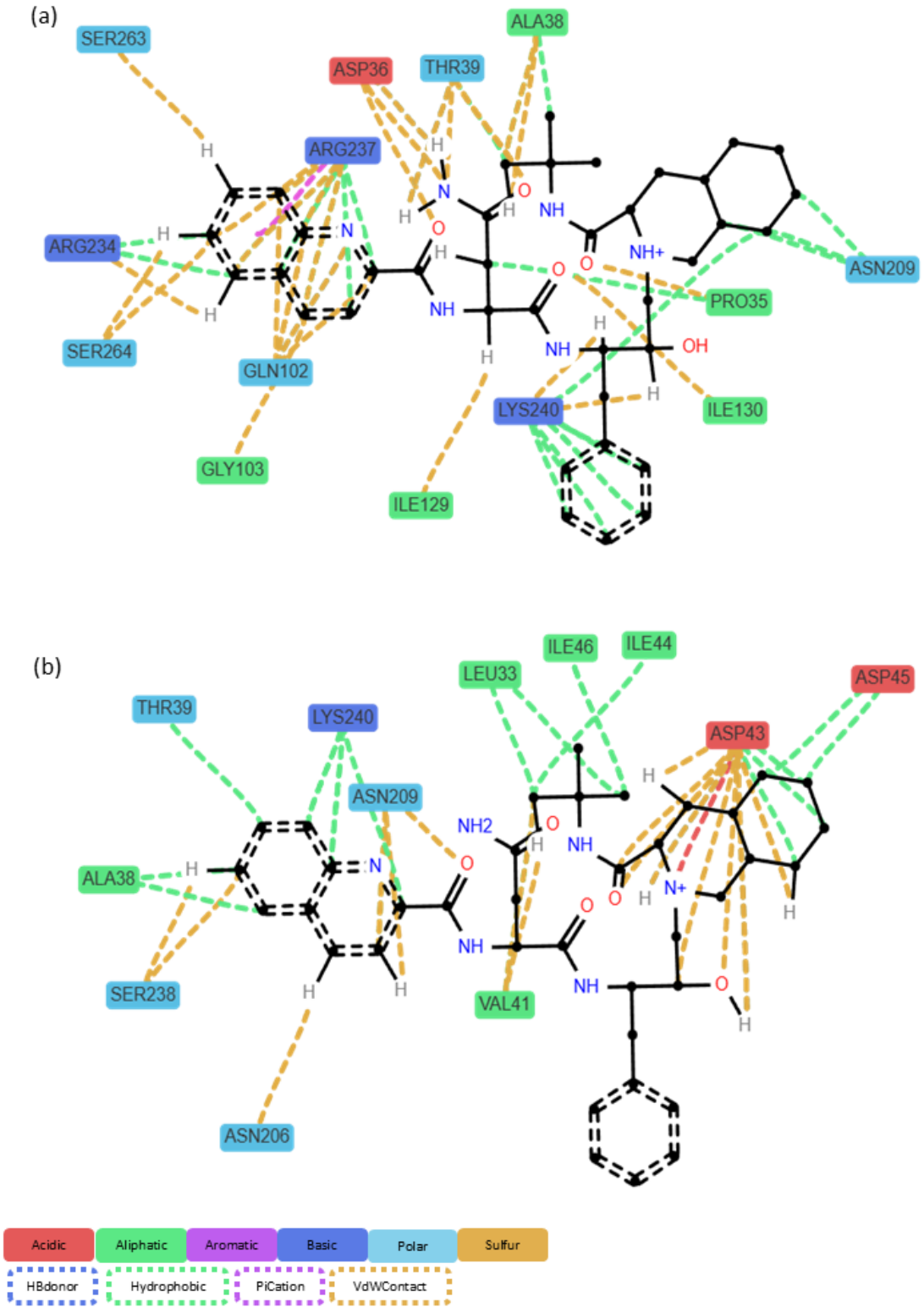

Figure 38: Interactions with residues in the Mutant 3 complex Saquinavir during frame 0 (a) and frame 1000 (b), respectively.

C.5 Comparison 2D Interaction Key Residue in Mutant 4 Complexes

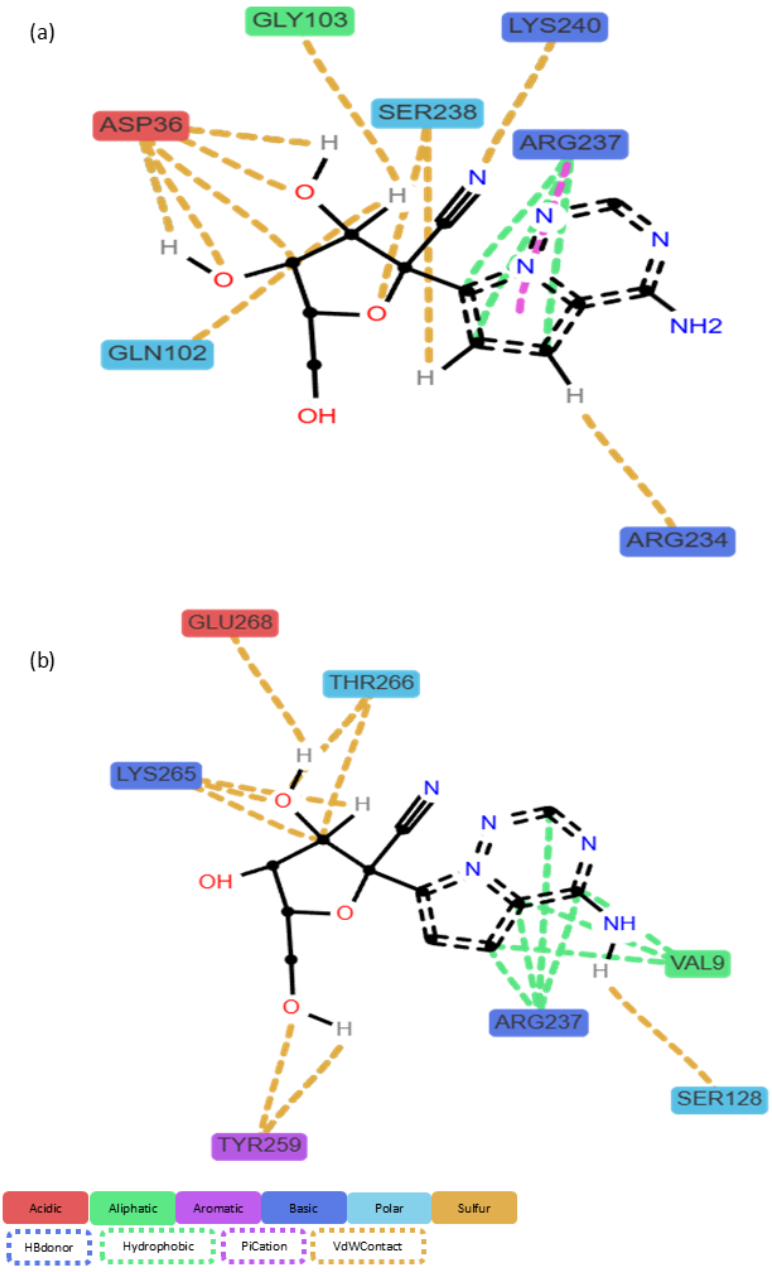

Figure 39: Interactions with residues in the Mutant 4 complex GS-441524 during frame 0 (a) and frame 1000 (b), respectively.

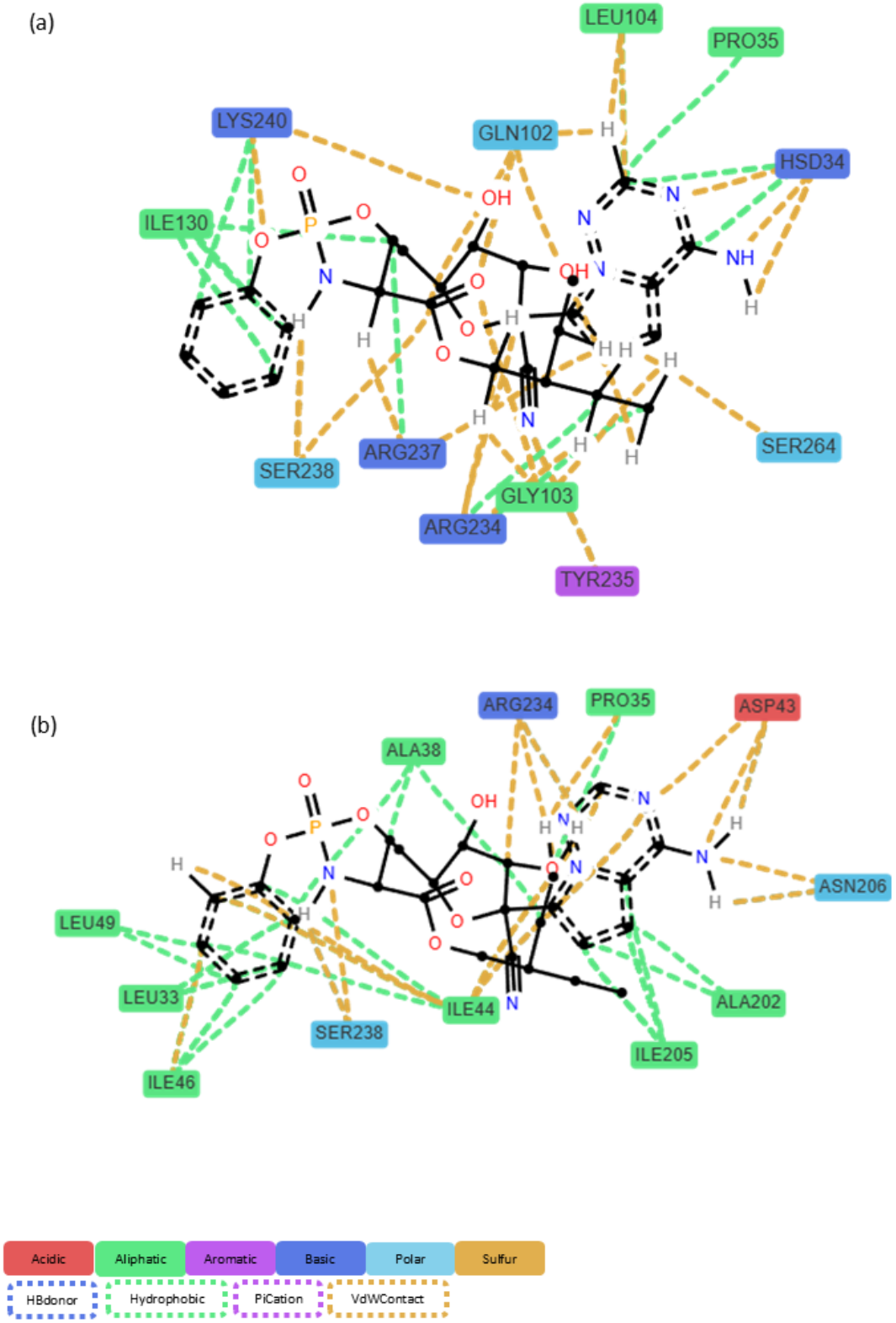

Figure 40: Interactions with residues in the Mutant 4 complex Remdesivir during frame 0 (a) and frame 1000 (b), respectively.

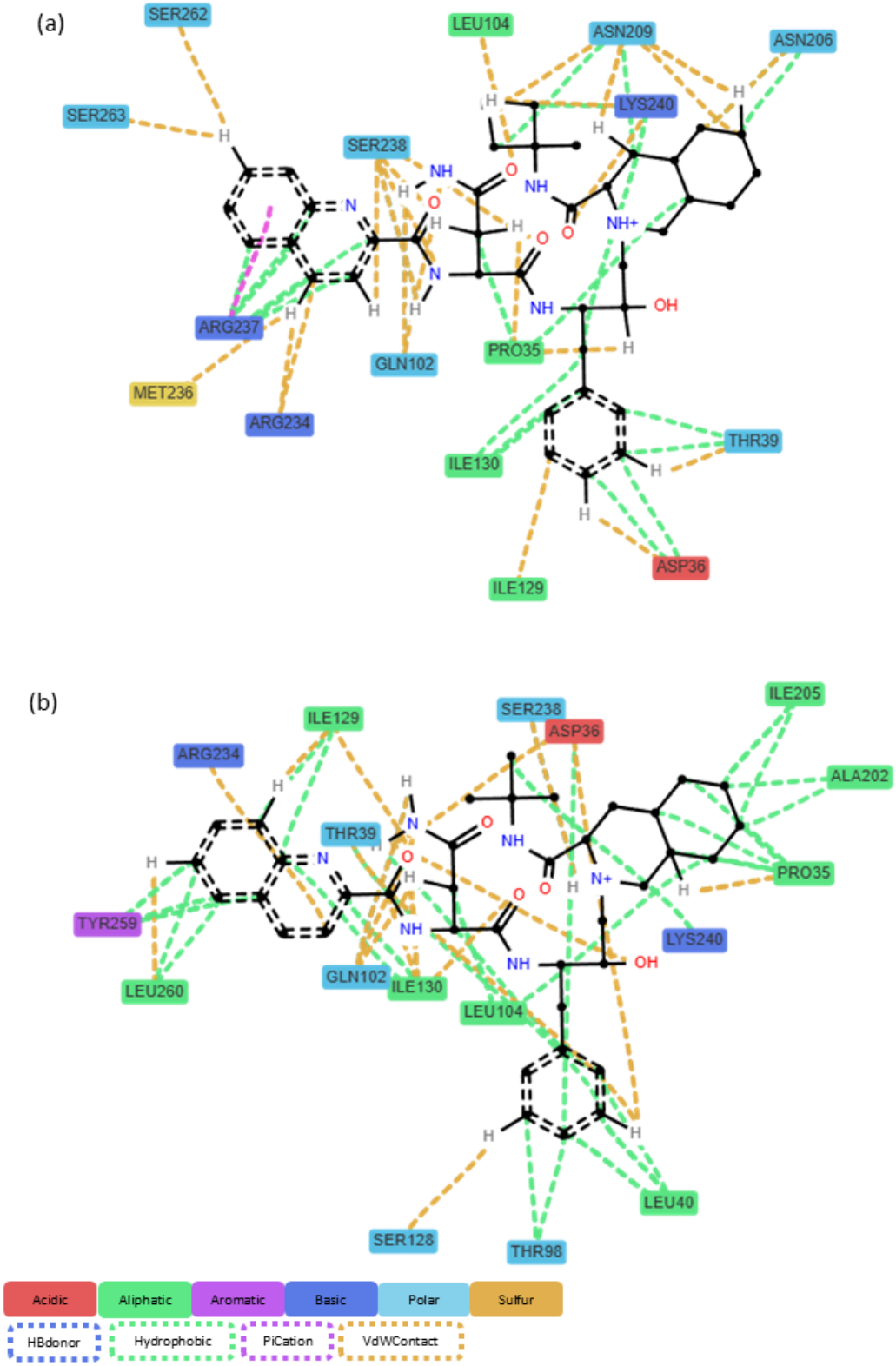

Figure 41: Interactions with residues in the Mutant 4 complex Saquinavir during frame 0 (a) and frame 1000 (b), respectively.

D Binding Free Energy of Contribution Mutated Nsp3-SUD and WT

D.1 Table Energy Decomposition Per-Residue With Inhibitor GS-441524

Table 3: Per-Residue Energy Decomposition for Wild-Type and Mutants 1-4 bound with GS-441524 (kcal/mol).

Residue	Wild-Type	Mutant 1	Mutant 2	Mutant 3	Mutant 4
PRO35	-0.18	-0.92	-0.79	-0.62	-0.81
ASP36	0.02	-2.34	-1.99	0.27	-2.36
THR39	-0.50	-0.09	-	-	-
GLN102	-0.35	-1.84	-1.49	-0.48	-1.44
GLY103	-0.26	-0.74	-0.52	-0.34	-0.08
LEU104	-0.50	-0.15	-	-0.76	-
SER128	-0.51	-0.92	-1.22	-0.02	-0.17
ILE129	-	-	0.001	-	-
ILE130	-0.91	-0.98	-0.80	-0.39	-0.54
ALA233	-	-0.14	-0.40	-	-0.06
ARG234	-0.91	-0.43	-1.10	-0.18	-0.16
TYR235	-0.05	-	-0.18	-0.03	-
MET236	-0.06	0.005	0.04	-006	-0.03
ARG237	-3.22	-2.94	-1.12	-1.80	-2.50
SER238	-0.59	-0.16	-0.18	-0.25	-0.06
LYS240	0.53	0.42	0.19	0.19	0.34
TYR259	-0.19	-0.03	-0.73	-0.12	-0.16
SER260	-	-0.17	-0.12	-	-0.43
SER262	-0.06	0.03	0.01	-0.10	-0.38
SER263	-0.07	-0.01	-0.02	-0.15	-0.29
SER264	-0.14	-0.06	-0.49	-0.22	0.01
TYR281	0.002	-0.009	0.002	-0.01	0.0007

D.2 Table Energy Decomposition Per-Residue With Inhibitor Remdesivir

Table 4: Per-Residue Energy Decomposition for Wild-Type and Mutants 1-4 bound with Remdesivir (kcal/mol).

Residue	Wild-Type	Mutant 1	Mutant 2	Mutant 3	Mutant 4
ASP28	0.13	0.28	-	0.06	0.01
ASN32	-0.16	-	-	-	-
LEU33	-0.47	-0.35	-	-	-
HSD34	-0.04	-0.64	-0.01	-0.003	0.001
PRO35	-0.83	-3.66	-1.47	-1.58	-0.18
ASP36	0.69	0.89		0.94	0.11
ALA38	-	-	-	-	-0.04
THR39	-0.48	-0.26	0.01	- -0.04	
THR73	-	-	0.03	0.01	-
LYS75	-	-	0.08	0.13	-
GLN102	-0.05	-0.21	-0.68	-0.89	-0.08
GLY103	-0.13	-0.75	-0.83	-0.40	-0.07
LEU104	-0.37	-2.34	-2.26	-0.48	-0.16
THR108	0.0008	-	-	-	-
VAL109	-	0.02	-	-0.15	-
SER128	0.02	0.07	-0.31	-0.13	-
ILE129	0.003	0.01	-0.19	-0.18	-
ILE130	-0.05	-0.01	-2.17	-1.48	-
SER131	-	-	-	-	0.01
ILE205	-1.10	-0.04	-0.32	-0.12	-0.14
ASN206	-0.67	0.03	-0.26	-0.01	-0.07
ASN209	-0.03	-0.01	-0.14	-0.08	-0.07
ALA233	-0.09	-0.38	-	0.003	-
ARG234	-1.44	-0.99	-1.32	-0.04	-0.002
TYR235	-1.40	-	-	-	-
MET236	0.02	-0.11	-	0.06	0.002
ARG237	-0.75	-2.97	-0.92	-2.18	-0.04
SER238	-1.35	-0.35	-1.77	-1.15	-0.10
LYS240	0.22	0.16	0.07	-1.15	-0.03
TYR259	-0.05	-0.21	0.01	0.003	-
LEU260	-0.15	-0.67	-	-0.07	-
SER262	0.02	-0.11	0.01	0.03	-
SER263	0.02	-0.12	0.01	0.02	-
SER264	0.04	0.10	0.001	0.037	-
TYR281	-0.03	-0.17	0.001	0.02	-

D.3 Table Energy Decomposition Per-Residue With Inhibitor Saquinavir

Table 5: Per-Residue Energy Decomposition for Wild-Type and Mutants 1-4 bound with Saquinavir (kcal/mol).

Residue	Wild-Type	Mutant 1	Mutant 2	Mutant 3	Mutant 4
ASN32	-	-	-	-0.43	-
LEU33	-	-	-	0.10	-
PRO35	-1.11	-0.88	-2.82	-2.40	-1.66
ASP36	-0.70	0.99	0.79	0.18	-007
ALA38	-	-0.99	-1.27	-	-
THR39	-1.96	-0.47	-0.88	0.04	-1.43
LYS75	-	-	0.11	-	-
GLN102	-1.10	-0.001	-2.58	-1.43	-0.89
GLY103	-0.68	-0.01	-0.85	-0.67	-019
LEU104	-2.31	-	-1.13	-3.67	-021
SER128	-0.66	-	-0.133	0.03	-0.84
ILE129	-2.44	-0.07	-0.11	-0.01	-198
ILE130	-3.59	-0.01	-1.03	-2.30	-2.25
SER131	-	-	-	0.35	-0007
ASN132	-	0.02	-	-0.17	0.02
ILE205	-1.13	-	-	-0.70	-0.69
ASN206	0.07	-	-	-0.18	-0.10
ASN209	-0.39	-0.83	-0.11	-	-1.00
ASP210	-	0.48	-	-	-
ASN212	0.02	-	0.01	-	0.003
ALA233	-0.32	-	-	-	-
ARG234	-0.91	0.02	-0.71	-1.16	-0.03
TYR235	-0.39	-0.06	-	-	-
MET236	-0.19	-	-	0.10	0.05
ARG237	-0.48	-0.13	-2.02	-3.77	-1.10
SER238	-1.20	-0.49	-0.56	-1.50	-2.28
LYS240	-0.17	-1.48	0.29	0.30	-129
VAL241	0.001	-	0.001	-	-0.11
TYR259	-0.53	-	-	-0.25	-0.02
SER262	0.01	0.01	-0.01	-0.21	0.02
SER263	0.004	0.009	-0.13	-0.70	0.02
SER264	0.002	0.01	-0.13	-0.29	0.01
TYR281	0.0001	-0.0001	0.001	-	0.002

E Table Comparison of Protein-Ligand Interaction Fingerprint Between Nsp3-SUD Wild-type and Mutation Complexes (%)

Table 6: Interaction Types per-residues for Wild-type and Mutants 1-4 bound with GS-441524 (%).

		Frequency				
Residue	**Interaction**	**Mutant 1**	**Mutant 2**	**Mutant 3**	**Mutant 4**	**Wild-Type**
ASP36	HBDonor	100.00	100.0	62.93	99.40	0.00
	VdWContact	100.00	100.0	63.73	99.50	0.00
GLN102	Hydrophobic	73.32	0.00	0.00	74.42	0.00
	VdWContact	43.45	59.04	37.36	57.64	0.00
GLY103	VdWContact	0.00	30.86	0.00	0.00	0.00
SER128	VdWContact	71.72	74.82	0.00	43.25	0.00
ILE130	VdWContact	37.36	0.00	0.00	0.00	0.00
MET234	Hydrophobic	0.00	70.02	0.00	0.00	0.00
	VdWContact	37.46	44.95	0.00	0.00	0.00
MET236	VdWContact	0.00	39.66	0.00	0.00	0.00
ARG237	Hydrophobic	78.62	0.00	0.00	93.50	95.10
	PiCation	92.40	0.00	57.24	88.71	50.84
	VdWContact	62.33	33.16	51.94	62.33	64.53
THR/ILE266	VdWContact	0.00	0.00	0.00	0.00	36.86

Table 7: Interaction Types per-residues for Wild-type and Mutants 1-4 bound with Remdesivir (%).

		Frequency				
Residue	**Interaction**	**Mutant 1**	**Mutant 2**	**Mutant 3**	**Mutant 4**	**Wild-Type**
PRO35	Hydrophobic	99.60	0.00	68.43	0.00	54.39
	VdWContact	64.63	32.06	0.00	0.00	0.00
ASP36	HBDonor	0.00	37.46	52.54	0.00	0.00
	VdWContact	0.00	42.82	53.24	0.00	0.00
GLN102	Hydrophobic	0.00	53.84	76.47	0.00	0.00
	VdWContact	0.00	35.06	53.14	0.00	0.00
GLY103	VdWContact	39.56	54.24	0.00	0.00	0.00
LEU104	Hydrophobic	95.30	90.30	0.00	0.00	0.00
	vdwContact	76.32	57.14	0.00	0.00	0.00
SER128	VdWContact	0.00	35.89	0.00	0.00	0.00
ILE130	Hydrophobic	0.00	94.40	73.47	0.00	0.00
	VdWContact	0.00	65.53	42.07	0.00	0.00
ILE205	Hydrophobic	0.00	0.00	0.00	0.00	90.51
	vdWContact	0.00	0.00	0.00	0.00	34.53
ASN206	HBDonor	0.00	0.00	0.00	0.00	82.83
	vdWContact	0.00	0.00	0.00	0.00	85.92
ARG234	HBDonor	0.00	0.00	0.00	0.00	61.77
	Hydrophobic	85.31	62.63	0.00	0.00	41.51
	VdWContact	40.95	47.15	0.00	0.00	75.84
TYR235	Hydrophobic	0.00	37.46	0.00	0.00	0.00
	VdWContact	0.00	0.00	0.00	0.00	56.78
ARG237	HBAcceptor	57.64	0.00	0.00	0.00	0.00
	Hydrophobic	48.35	69.33	86.64	0.00	30.53
	VdWContact	77.62	45.25	67.79	0.00	45.60
SER238	VdWContact	34.56	87.61	64.40	0.00	77.74
LYS240	Hydrophobic	0.00	30.36	73.97	0.00	0.00
	VdWContact	0.00	0.00	50.24	0.00	0.00

Table 8: Interaction Types per-residues for Wild-type and Mutants 1-4 bound with Saquinavir (%).

		Frequency				
Residue	**Interaction**	**Mutant 1**	**Mutant 2**	**Mutant 3**	**Mutant 4**	**Wild-Type**
PRO35	Hydrophobic	43.75	82.57	68.43	80.41	87.41
	VdWContact	0.00	72.98	53.34	40.15	35.76
ASP36	HBAcceptor	0.00	0.00	45.65	0.00	0.00
	HBDonor	0.00	0.00	60.83	0.00	0.00
	Hydrophobic	0.00	0.00	0.00	80.31	89.01
	VdWContact	0.00	0.00	79.92	42.05	47.55
ALA38	Hydrophobic	92.00	98.59	0.00	0.00	0.00
	vdwContact	37.66	44.67	0.00	0.00	0.00
THR39	Hydrophobic	0.00	70.87	0.00	89.51	91.3
	vdwContact	34.76	38.47	0.00	52.74	69.63
GLN102	HBDonor	0.00	83.97	94.10	0.00	93.00
	Hydrophobic	0.00	65.38	57.54	52.94	0.00
	VdWContact	0.00	95.43	97.20	0.00	98.00
GLY103	HBAcceptor	0.00	59.29	0.00	0.00	0.00
	VdWContact	0.00	85.49	0.00	0.00	0.00
LEU104	Hydrophobic	0.00	58.12	98.50	0.00	99.40
	VdWContact	0.00	0.00	80.61	0.00	50.64
SER128	HBDonor	0.00	0.00	0.00	61.03	0.00
	VdWContact	0.00	0.00	0.00	76.22	83.71
ILE129	Hydrophobic	0.00	0.00	0.00	87.61	44.85
	vdWContact	0.00	0.00	0.00	58.94	55.94
ILE130	HBAcceptor	0.00	0.00	0.00	0.00	55.94
	Hydrophobic	0.00	30.52	98.10	92.30	96.60
	VdWContact	0.00	32.28	61.73	70.22	87.21
ILE205	Hydrophobic	0.00	0.00	83.11	76.22	94.20
ASN206	HBAcceptor	0.00	0.00	0.00	0.00	55.94
ASN209	Hydrophobic	0.00	0.00	0.00	95.10	0.00
	vdWContact	0.00	0.00	0.00	47.65	0.00
ARG234	Hydrophobic	0.00	71.46	46.05	0.00	0.00
	VdWContact	0.00	0.00	0.00	0.00	47.35
TYR235	Hydrophobic	0.00	0.00	75.82	0.00	0.00
	VdWContact	0.00	0.00	30.96	0.00	0.00
ARG237	HBAcceptor	0.00	38.12	0.00	0.00	0.00
	Hydrophobic	0.00	94.85	97.50	88.61	0.00
	PiCation	0.00	31.92	0.00	0.00	0.00
	VdWContact	0.00	70.87	92.50	44.75	0.00
SER238	HBDonor	0.00	0.00	0.00	51.54	66.23
	VdWContact	0.00	34.38	73.02	92.40	90.50
LYS240	HBAcceptor	0.00	0.00	0.00	0.00	0.00
	Hydrophobic	95.40	33.45	0.00	73.32	82.81
	VdWContact	66.63	0.00	0.00	46.35	30.16
SER264	VdWContact	0.00	0.00	35.76	0.00	0.00
THR/ILE266	Hydrophobic	0.00	0.00	70.02	0.00	0.00

References

[1] N. Z. Zabidi, H. L. Liew, I. A. Farouk, A. Puniyamurti, A. J. W. Yip, V. N. Wijesinghe, Z. Y. Low, J. W. Tang, V. T. K. Chow, S. K. Lal, Evolution of sars-cov-2 variants: Implications on immune escape, vaccination, therapeutic and diagnostic strategies, Viruses 15 (4) (2023) 944. doi:10.3390/v15040944.
URL http://dx.doi.org/10.3390/v15040944

[2] S. Zhand, M. Saghaeian Jazi, S. Mohammadi, R. Tarighati Rasekhi, G. Rostamian, M. R. Kalani, A. Rostamian, J. George, M. W. Douglas, Covid-19: The immune responses and clinical therapy candidates, International Journal of Molecular Sciences 21 (15) (2020) 5559. doi:10.3390/ijms21155559.
URL http://dx.doi.org/10.3390/ijms21155559

[3] W. W. Harless, B. Lewis, B. Qorri, S. Abdulkhalek, M. R. Szewczuk, Novel therapeutic target critical for sars-cov-2 infectivity and induction of the cytokine release syndrome, Cells 12 (9) (2023) 1332. doi:10.3390/cells12091332.
URL http://dx.doi.org/10.3390/cells12091332

[4] K. Solanki, S. Rajpoot, A. Kumar, K. Y. J Zhang, T. Ohishi, N. Hirani, K. Wadhonkar, P. Patidar, Q. Pan, M. S. Baig, Structural analysis of spike proteins from sars-cov-2 variants of concern highlighting their functional alterations, Future Virology 17 (10) (2022) 723–732. doi:10.2217/fvl-2022-0003.
URL http://dx.doi.org/10.2217/fvl-2022-0003

[5] H. J. C. Berendsen, J. P. M. Postma, W. F. van Gunsteren, A. DiNola, J. R. Haak, Molecular dynamics with coupling to an external bath, The Journal of Chemical Physics 81 (8) (1984) 3684–3690. doi:10.1063/1.448118.
URL http://dx.doi.org/10.1063/1.448118

[6] W. Yan, Y. Zheng, X. Zeng, B. He, W. Cheng, Structural biology of sars-cov-2: open the door for novel therapies, Signal Transduction and Targeted Therapy 7 (1) (Jan. 2022). doi:10.1038/s41392-022-00884-5.
URL http://dx.doi.org/10.1038/s41392-022-00884-5

[7] R. Gorkhali, P. Koirala, S. Rijal, A. Mainali, A. Baral, H. K. Bhattarai, Structure and function of major sars-cov-2 and sars-cov proteins, Bioinformatics and Biology Insights 15 (2021) 117793222110258. doi:10.1177/11779322211025876.
URL http://dx.doi.org/10.1177/11779322211025876

[8] P. Li, B. Xue, N. J. Schnicker, L.-Y. R. Wong, D. K. Meyerholz, S. Perlman, Nsp3-n interactions are critical for sars-cov-2 fitness and virulence, Proceedings of the National Academy of Sciences 120 (31) (Jul. 2023). doi:10.1073/pnas.2305674120.
URL http://dx.doi.org/10.1073/pnas.2305674120

[9] J. Lei, Y. Ma-Lauer, Y. Han, M. Thoms, R. Buschauer, J. Jores, V. Thiel, R. Beckmann, W. Deng, H. Leonhardt, R. Hilgenfeld, A. von Brunn, The sars-unique domain (sud) of sars-cov and sars-cov-2 interacts with human paip1 to enhance viral rna translation, The EMBO Journal 40 (11) (Apr. 2021). doi:10.15252/embj.2019102277.
URL http://dx.doi.org/10.15252/embj.2019102277

[10] M. H. Abbasian, M. Mahmanzar, K. Rahimian, B. Mahdavi, S. Tokhanbigli, B. Moradi, M. M. Sisakht, Y. Deng, Global landscape of sars-cov-2 mutations and conserved regions, Journal of Translational Medicine 21 (1) (Feb. 2023). doi:10.1186/s12967-023-03996-w.
URL http://dx.doi.org/10.1186/s12967-023-03996-w

[11] C. K. V. Nonaka, M. M. Franco, T. Gräf, C. A. de Lorenzo Barcia, R. N. de Ávila Mendonça, K. A. F. de Sousa, L. M. C. Neiva, V. Fosenca, A. V. A. Mendes, R. S. de Aguiar, M. Giovanetti, B. S. de Freitas Souza, Genomic evidence of sars-cov-2 reinfection involving e484k spike mutation, brazil, Emerging Infectious Diseases 27 (5) (2021) 1522–1524. doi:10.3201/eid2705.210191.
URL http://dx.doi.org/10.3201/eid2705.210191

[12] T. A. Hopf, J. B. Ingraham, F. J. Poelwijk, C. P. I. Schärfe, M. Springer, C. Sander, D. S. Marks, Mutation effects predicted from sequence co-variation, Nature Biotechnology 35 (2) (2017) 128–135. doi:10.1038/nbt.3769.
URL http://dx.doi.org/10.1038/nbt.3769

[13] K. Habler, M. Brügel, D. Teupser, U. Liebchen, C. Scharf, U. Schönermarck, M. Vogeser, M. Paal, Simultaneous quantification of seven repurposed covid-19 drugs remdesivir (plus metabolite gs-441524), chloroquine, hydroxychloroquine, lopinavir, ritonavir, favipiravir and azithromycin by a two-dimensional isotope dilution lc–ms/ms method in human serum, Journal of Pharmaceutical and Biomedical Analysis 196 (2021) 113935. doi:10.1016/j.jpba.2021.113935.
URL http://dx.doi.org/10.1016/j.jpba.2021.113935

[14] T. Sato, M. Maekawa, N. Mano, T. Abe, H. Yamaguchi, Role of oatp4c1 in renal handling of remdesivir and its nucleoside analog gs-441524: The first approved drug for patients with covid-19, Journal of Pharmacy amp; Pharmaceutical Sciences 24 (2021) 227–236. doi:10.18433/jpps31813.
URL http://dx.doi.org/10.18433/jpps31813

[15] S. Cherian, P. Yadav, V. Potdar, M. Choudhary, D. Nyayanit, M. Agrawal, S. Jadhav, T. Majumdar, A. Shete-Aich, A. Basu, P. Abraham, Full-genome sequences of the first two sars-cov-2 viruses from india, Indian Journal of Medical Research 151 (2) (2020) 200. doi:10.4103/ijmr.$ijmr_6 63_2 0$.
URL http://dx.doi.org/10.4103/ijmr.$IJMR_6 63_2 0$

[16] Re3data.Org, Gisaid (2012). doi:10.17616/R3Q59F.
URL https://www.re3data.org/repository/r3d100010126

[17] K. Okonechnikov, O. Golosova, M. Fursov, Unipro ugene: a unified bioinformatics toolkit, Bioinformatics 28 (8) (2012) 1166–1167. doi:10.1093/bioinformatics/bts091.
URL http://dx.doi.org/10.1093/bioinformatics/bts091

[18] K. Katoh, D. M. Standley, Mafft multiple sequence alignment software version 7: Improvements in performance and usability, Molecular Biology and Evolution 30 (4) (2013) 772–780. doi:10.1093/molbev/mst010.
URL http://dx.doi.org/10.1093/molbev/mst010

[19] H. Land, M. S. Humble, YASARA: A Tool to Obtain Structural Guidance in Biocatalytic Investigations, Springer New York, 2017, p. 43–67. doi:10.1007/978-1-4939-7366-8_4.
URL http://dx.doi.org/10.1007/978-1-4939-7366-8_4

[20] E. F. Pettersen, T. D. Goddard, C. C. Huang, G. S. Couch, D. M. Greenblatt, E. C. Meng, T. E. Ferrin, Ucsf chimera—a visualization system for exploratory research and analysis, Journal of Computational Chemistry 25 (13) (2004) 1605–1612. doi:10.1002/jcc.20084.
URL http://dx.doi.org/10.1002/jcc.20084

[21] X. Zhou, W. Zheng, Y. Li, R. Pearce, C. Zhang, E. W. Bell, G. Zhang, Y. Zhang, I-tasser-mtd: a deep-learning-based platform for multi-domain protein structure and function prediction, Nature Protocols 17 (10) (2022) 2326–2353. doi:10.1038/s41596-022-00728-0.
URL http://dx.doi.org/10.1038/s41596-022-00728-0

[22] S. Jo, T. Kim, V. G. Iyer, W. Im, Charmm-gui: A web-based graphical user interface for charmm, Journal of Computational Chemistry 29 (11) (2008) 1859–1865. doi:10.1002/jcc.20945.
URL http://dx.doi.org/10.1002/jcc.20945

[23] J. Lee, X. Cheng, J. M. Swails, M. S. Yeom, P. K. Eastman, J. A. Lemkul, S. Wei, J. Buckner, J. C. Jeong, Y. Qi, S. Jo, V. S. Pande, D. A. Case, C. L. Brooks, A. D. MacKerell, J. B. Klauda, W. Im, Charmm-gui input generator for namd, gromacs, amber, openmm, and charmm or openmm simulations using the charmm36 additive force field, Journal of Chemical Theory and Computation 12 (1) (2015) 405–413. doi:10.1021/acs.jctc.5b00935.
URL http://dx.doi.org/10.1021/acs.jctc.5b00935

[24] P. Bauer, B. Hess, E. Lindahl, Gromacs 2022.2 source code (2022). doi:10.5281/ZENODO.6637571.
URL https://zenodo.org/record/6637571

[25] R. Gowers, M. Linke, J. Barnoud, T. Reddy, M. Melo, S. Seyler, J. Domański, D. Dotson, S. Buchoux, I. Kenney, O. Beckstein, Mdanalysis: A python package for the rapid analysis of molecular dynamics simulations, in: Proceedings of the 15th Python in Science Conference, SciPy, SciPy, 2016, p. 98–105. doi:10.25080/majora-629e541a-00e.
URL http://dx.doi.org/10.25080/majora-629e541a-00e

[26] N. Michaud-Agrawal, E. J. Denning, T. B. Woolf, O. Beckstein, Mdanalysis: A toolkit for the analysis of molecular dynamics simulations, Journal of Computational Chemistry 32 (10) (2011) 2319–2327. doi:10.1002/jcc.21787.
URL http://dx.doi.org/10.1002/jcc.21787

[27] S. Kim, H. Oshima, H. Zhang, N. R. Kern, S. Re, J. Lee, B. Roux, Y. Sugita, W. Jiang, W. Im, Charmm-gui free energy calculator for absolute and relative ligand solvation and binding free energy simulations, Journal of Chemical Theory and Computation 16 (11) (2020) 7207–7218. doi:10.1021/acs.jctc.0c00884.
URL http://dx.doi.org/10.1021/acs.jctc.0c00884

[28] W. L. Jorgensen, The many roles of computation in drug discovery, Science 303 (5665) (2004) 1813–1818. doi:10.1126/science.1096361.
URL http://dx.doi.org/10.1126/science.1096361

[29] Y. Deng, B. Roux, Calculation of standard binding free energies: Aromatic molecules in the t4 lysozyme l99a mutant, Journal of Chemical Theory and Computation 2 (5) (2006) 1255–1273. doi:10.1021/ct060037v.
URL http://dx.doi.org/10.1021/ct060037v

[30] Z. Cournia, B. K. Allen, T. Beuming, D. A. Pearlman, B. K. Radak, W. Sherman, Rigorous free energy simulations in virtual screening, Journal of Chemical Information and Modeling 60 (9) (2020) 4153–4169. doi:10.1021/acs.jcim.0c00116.
URL http://dx.doi.org/10.1021/acs.jcim.0c00116

[31] E. Wang, H. Sun, J. Wang, Z. Wang, H. Liu, J. Z. H. Zhang, T. Hou, End-point binding free energy calculation with mmpbsa and mmgbsa: Strategies and applications in drug design, Chemical Reviews 119 (16) (2019) 9478–9508. doi:10.1021/acs.chemrev.9b00055.
URL http://dx.doi.org/10.1021/acs.chemrev.9b00055

[32] J. Weiser, P. S. Shenkin, W. C. Still, Approximate atomic surfaces from linear combinations of pairwise overlaps lcpo, Journal of Computational Chemistry 20 (2) (1999) 217–230. doi:10.1002/(sici)1096-987x(19990130)20:2¡217::aid-jcc4¿3.0.co;2-a.
URL http://dx.doi.org/10.1002/(SICI)1096-987X(19990130)20:2<217::AID-JCC4>3.0.CO;2-A

[33] A. Onufriev, D. Bashford, D. A. Case, Exploring protein native states and large-scale conformational changes with a modified generalized born model, Proteins: Structure, Function, and Bioinformatics 55 (2) (2004) 383–394. doi:10.1002/prot.20033.
URL http://dx.doi.org/10.1002/prot.20033

[34] L. Xu, H. Sun, Y. Li, J. Wang, T. Hou, Assessing the performance of mmpbsa and mmgbsa methods. 3. the impact of force fields and ligand charge models, The Journal of Physical Chemistry B 117 (28) (2013) 8408–8421. doi:10.1021/jp404160y.
URL http://dx.doi.org/10.1021/jp404160y

[35] T. Hou, J. Wang, Y. Li, W. Wang, Assessing the performance of the mmpbsa and mmgbsa methods. 1. the accuracy of binding free energy calculations based on molecular dynamics simulations, Journal of Chemical Information and Modeling 51 (1) (2010) 69–82. doi:10.1021/ci100275a.
URL http://dx.doi.org/10.1021/ci100275a

[36] B. Qin, Z. Li, K. Tang, T. Wang, Y. Xie, S. Aumonier, M. Wang, S. Yuan, S. Cui, Identification of the sars-unique domain of sars-cov-2 as an antiviral target, Nature Communications 14 (1) (Jul. 2023). doi:10.1038/s41467-023-39709-6.
URL http://dx.doi.org/10.1038/s41467-023-39709-6

[37] L.-Y. Zhai, A.-M. Su, J.-F. Liu, J.-J. Zhao, X.-G. Xi, X.-M. Hou, Recent advances in applying g-quadruplex for sars-cov-2 targeting and diagnosis: A review, International Journal of Biological Macromolecules 221 (2022) 1476–1490. doi:10.1016/j.ijbiomac.2022.09.152.
URL http://dx.doi.org/10.1016/j.ijbiomac.2022.09.152